Atmospheric
Measurement
Techniques

CALOTRITON: a convective boundary layer height estimation algorithm from ultra-high-frequency (UHF) wind profiler data

Alban Philibert[1,2], Marie Lothon[2], Julien Amestoy[3], Pierre-Yves Meslin[1], Solène Derrien[2], Yannick Bezombes[2], Bernard Campistron[2], Fabienne Lohou[2], Antoine Vial[2], Guylaine Canut-Rocafort[4], Joachim Reuder[5], and Jennifer K. Brooke[6]

[1]Institut de Recherche en Astrophysique et Planétologie, Université de Toulouse, CNRS, UPS, Toulouse, France
[2]Laboratoire d'Aérologie, Université de Toulouse, CNRS, UPS, Toulouse, France
[3]CEA, DAM, DIF, 91297 Arpajon, France
[4]CNRM – Université de Toulouse, Météo-France/CNRS, Toulouse, France
[5]Geophysical Institute, and Bergen Offshore Wind Centre, University of Bergen,
and Bjerknes Centre for Climate Research, Bergen, Norway
[6]Met Office, Fitzroy Road, Exeter, EX1 3PB, UK

Correspondence: Marie Lothon (marie.lothon@aero.obs-mip.fr)

Abstract. Long time series of observations of atmospheric dynamics and composition are collected at the French Pyrenean Platform for Observation of the Atmosphere (P2OA). Planetary boundary layer depth is a key variable of the climate system, but it remains difficult to estimate and analyse statistically. In order to obtain reliable estimates of the convective boundary layer height (Z_i) and to allow long-term series analyses, a new restitution algorithm, named CALOTRITON, has been developed. It is based on the observations of an ultra-high-frequency (UHF) radar wind profiler (RWP) from P2OA with the help of other instruments for evaluation. Estimates of Z_i are based on the principle that the top of the convective boundary layer is associated with both a marked inversion and a decrease in turbulence. Those two criteria are respectively manifested by larger RWP reflectivity and smaller vertical-velocity Doppler spectral width. With this in mind, we introduce a new UHF-deduced dimensionless parameter which weighs the air refractive index structure coefficient with the inverse of vertical velocity standard deviation to the power of x. We then search for the most appropriate local maxima of this parameter for Z_i estimates with defined criteria and constraints such as temporal continuity. Given that Z_i should correspond to fair-weather cloud base height, we use ceilometer data to optimize our choice of the power x and find that $x = 3$ provides the best comparisons. The estimates of Z_i by CALOTRITON are evaluated using different Z_i estimates deduced from radiosounding according to different definitions. The comparison shows excellent results with a regression coefficient of up to 0.96 and a root-mean-square error of 71 m, which is close to the vertical resolution of the UHF RWP of 75 m, when conditions are optimal. In more complex situations, that is when the atmospheric vertical structure is itself particularly ambiguous, secondary retrievals allow us to identify potential thermal internal boundary layers or residual layers and help to qualify the Z_i estimations. Frequent estimate errors are observed nevertheless; for example, when Z_i is below the UHF RWP first reliable gate or when the boundary layer begins its transition to a stable nocturnal boundary layer.

1 Introduction

1.1 Instrumental techniques for convective boundary layer retrieval

The convective boundary layer (CBL) depth (Z_i) is a key variable in the climate system for its role in modulating energy, water, and trace species exchange at the interface between the surface and free atmosphere. For this reason, it has

significant applications in the fields of air quality, numerical weather predictions, climate models, and applied sectors such as renewable energy production. There are challenges in understanding the role of the convective boundary layer over heterogeneous surfaces; in complex terrains, coastal areas, and polar regions; and for surface–atmospheric exchange, transport, and mesoscale circulation, all of which require a comprehensive estimate of the CBL depth. Nevertheless, it remains difficult to accurately and exhaustively quantify it in the real world in terms of both the spatial and temporal variability due to its complexity.

Instrumental techniques for Z_i retrieval are numerous and have led to an abundance of literature. Kotthaus et al. (2023) propose a recent overview of the CBL top detection techniques with an exhaustive description of their capabilities and limitations. Here we summarize the most relevant techniques applicable to this study.

There are several ways to identify Z_i based on its characteristic atmospheric processes, which can be used to define different observational techniques. They can be classified into three main approaches based on the (i) thermodynamical processes, (ii) turbulent processes, and (iii) tracers. Figure 1 schematizes those various definitions through the vertical profiles of key variables.

The thermodynamical approach considers Z_i to be the height from the surface at which the summital inversion occurs, characterized by strong gradients of temperature and moisture (Fig. 1a, b). Several instrumental methods estimate Z_i based on this approach, such as

– the detection of the gradients of either the potential temperature, relative humidity (RH), or water vapour mixing ratio (e.g. Hennemuth and Lammert, 2006);

– the detection of the maximum of relative humidity (Couvreux et al., 2016);

– the so-called parcel method, which considers the potential temperature (or virtual potential temperature) at the surface θ_s and searches for the height above the surface where $\theta = \theta_s$ (Holzworth, 1964) or $\theta = \theta_s + \delta\theta$, where $\delta\theta$ is a small positive variation in surface potential temperature (Seibert et al., 2000).

In situ measurements from radiosounding, aircraft, or remotely piloted aircraft systems (RPASs) can be used based on this approach. Remote sensing provides an indirect measure of thermodynamical variables such as microwave radiometers, Raman lidar, or differential absorption lidar. Indirectly related to this approach, ultra-high-frequency (UHF) radar wind profilers (RWPs) in L-band are also appropriate devices to detect the CBL summital inversion, which is associated with a significant increase in reflectivity (White, 1993; Angevine et al., 1994).

Approaches based on turbulent processes consider Z_i to be the height from the surface where turbulence intensity starts

to strongly decrease (Fig. 1e). This height is coupled with the minimum (and negative) buoyancy flux (Deardorff, 1972) and a decrease in vertical velocity variance (Stull, 1988), turbulence kinetic energy (TKE), or TKE dissipation rate (ε). Both buoyancy flux and vertical velocity variance reach zero above Z_i in textbook cases (unforced conditions and clear air). However, in cases of external forcing such as clouds, wind shear, or advection, a local minimum can be observed on each profile (see the red line in Fig. 1e, f). Doppler lidar and UHF RWPs give information on the turbulence intensity (Frehlich et al., 2006; Jacoby-Koaly et al., 2002, respectively). The variance of the Doppler velocity (Lothon et al., 2006) or the turbulence kinetic energy dissipation rate (e.g. Frehlich et al., 2006) can be used to detect the CBL top based on a threshold. Note that studies based on numerical weather predictions models often use TKE as a reference for Z_i determination (Couvreux et al., 2016), whereas studies based on large eddy simulation often consider the minimum of the buoyancy flux (e.g. Pino et al., 2006). This makes those turbulence-based approaches very relevant for model evaluation.

The tracer-based approach considers Z_i to be the height from the surface where strong discontinuity is observed in scalar concentration profiles (Fig. 1d) such as aerosol or gas concentration. Optical remote sensing such as lidar and ceilometers measure the optical backscatter coefficient from which aerosol concentration can be inferred (see Kotthaus et al., 2023, for an exhaustive list). Wavelet methods are typically used to detect the top of the more loaded CBL (e.g. Haeffelin et al., 2012), where the aerosol concentration abruptly falls from the CBL to the free troposphere (see e.g. Davis et al., 2000, for the use of the Haar-wavelet-based method). The mixing ratio maximum gradient method described above could also be considered a scalar concentration approach.

Some approaches use the synergy of instruments or methods. The bulk Richardson method (Hanna, 1969), with a threshold on the gradient Richardson number, is a combination of the wind gradient and the potential temperature gradient. The complementarity of instruments is widely used for Z_i estimations. For example, Min et al. (2020) or Turner and Lohnert (2021) use the association of a microwave radiometer with a ceilometer or Raman lidar respectively. Since they are based on different definitions, all the methods discussed potentially result in slightly different estimates of Z_i (Caicedo et al., 2017), especially when the observed CBL is not a simple idealized case.

In this study, we revisit the methodology of estimating Z_i from UHF RWP measurements and propose a new complementary algorithm. The advantage of RWPs relative to other remote sensing devices is their ability to measure in all weather types and not be limited by cloud types and the amount thereof, precipitation, or clear-sky conditions. Their height coverage limitation is predominately related due to water vapour content. One known weakness is their sensitivity to bird echoes, which typically occur in the nighttime
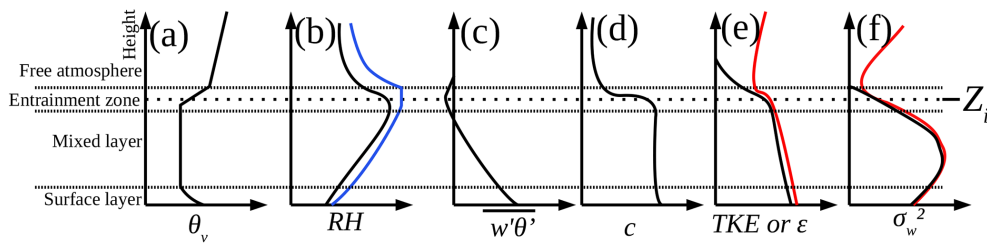
Figure 1. Idealized CBL profiles (black line) of the **(a)** potential temperature, **(b)** relative humidity (blue line indicates the situation in the presence of clouds), **(c)** buoyancy flux, **(d)** scalar concentration, **(e)** turbulence kinetic energy (TKE) or TKE dissipation rate (ε), and **(f)** vertical velocity variance (red line indicates the situation in the presence of external forcing).

during bird migration events, particularly in spring and autumn. It is usually not a significant issue during daytime convection.

1.2 Motivations and main objectives

The multi-instrumented site of the ACTRIS-Fr[1] infrastructure, the Pyrenean Platform for Observation of the Atmosphere (P2OA[2] – Lothon et al., 2024), gathers a comprehensive set of instruments for the monitoring of the atmosphere, with a subselection of instrumentation located at the Centre de Recherches Atmosphériques (CRA), Campistrous, in south-west France, close to the Pyrenees mountain ridge. Among them, a UHF RWP purchased by the LAERO[3] laboratory has continuously measured the boundary layer since 2010. Retrieving the CBL height from this instrument from this multi-year time series allows for a statistical study of the dynamical processes in this mountainous region. These processes include the influence of plain–mountain circulations and thermally driven winds, the interaction between mountain waves and the boundary layer, and the impact of mesoscale subsidence related to orographic convection. This unique dataset enables us to make statistical analyses and climatologies, with applications in air quality, weather forecasting, and climate studies.

An existing technique, partly based on Angevine et al. (1994), was used for this specific radar to estimate Z_i (Jacoby-Koaly et al., 2002). Angevine et al. (1994) base the estimate of Z_i on the absolute maximum of the air refractive index structure coefficient (C_n^2), which, however, does not always correspond to the current CBL top but can correspond to the residual inversion above. To address this, Jacoby-Koaly et al. (2002) attempted to retrieve the local maximum of C_n^2 that could be the most appropriate estimate of Z_i by using temporal continuity and other criteria. This is also the approach of Collaud Coen et al. (2014). Note that

C_n^2 reaches local maxima where temperature and humidity show not only large vertical gradients, but also large wind gradients and turbulence (which induces fluctuations in the air refractive index). This technique provides very satisfying results on a case-by-case investigation for fair-weather convective conditions without the complex vertical structure of the atmosphere (Heo et al., 2003; Jacoby-Koaly, 2000). However, statistical studies of the time series based on this technique may not be possible without significant errors. One obvious limitation, for example, is that it often catches the top of the residual layer in the early morning rather than the top of the shallower developing CBL top. The temporal continuity criterion does not solve this issue. Attributing Z_i to the top of the residual layer during the morning transition potentially leads to large errors. This can also occur in late afternoon, when this method will likely attribute Z_i to the top of the pre-residual layer (Nilsson et al., 2016b) and then residual layer, while true Z_i may decay with the decreasing surface heat flux and decaying turbulence layer (Grimsdell and Angevine, 2002; Lothon et al., 2014). It can also catch upper inversions, which are not directly connected to the mixed layer. Also note that residual layers are not always a local phenomenon but may be advected (Angevine, 2000). In the presence of clouds at different levels, the difficulties increase due to more complexity, with greater stratification of the atmosphere and in cloud turbulence (Grimsdell and Angevine, 1998; Angevine, 2000; Collaud Coen et al., 2014; Duncan et al., 2022).

Several other techniques are based on the same principle of the existence of a local maximum of reflectivity. For example, Liu et al. (2019) use local maxima of normalized signal-to-noise ratio (SNR); Compton et al. (2013) use the covariance wavelet transform to detect the large step in SNR associated with Z_i; and Molod et al. (2015) use a simple algorithm with the use of SNR, based on the determination of the "emergence time", and corresponding height and temporal continuity, based on backscatter standard deviation. All of them, however, encounter the same difficulties mentioned above, to a greater or lesser extent. Molod et al. (2015) used this technique to retrieve long series of Z_i from a network of profilers, but the departure from in situ estimates based

on the bulk Richardson number shows that although simple and significantly robust, the proposed algorithm still cannot handle the high complexity of the low troposphere. Collaud Coen et al. (2014) developed a climatology of the CBL height based on multiple remote sensing instruments and validated the dataset against radiosoundings. They found that their estimates from the RWP were more dispersed due to false attributions, revealing the difficulty of this approach when dealing with the various encountered conditions.

One way to improve this method is to also consider the decrease in turbulence at the top of the convective layer (see Fig. 1e, f) combined with the association to a local maximum of C_n^2 (Heo et al., 2003) or SNR (Bianco and Wilczak, 2002; Bianco et al., 2008). Heo et al. (2003) assume that the zero buoyancy flux is reached where the vertical velocity standard deviation is null. They search for this height and then select the nearest local maximum of C_n^2. With the same basic assumption, Bianco and Wilczak (2002) and Bianco et al. (2008) use the fuzzy logic method to determine the height which corresponds to the combination of radar variables. Those techniques definitely improve the CBL depth estimates relatively to the more standard approaches.

In this study, we use this same fundamental assumption and combination to improve the initial method used for the LAERO UHF RWP radar in order to develop a new algorithm to address a broader range of atmospheric conditions, including the complex vertical structure of the atmosphere, cloudy situations, and multilayered lower troposphere.

We present the experimental data used in Sect. 2, and we describe the Z_i-retrieval algorithm (CALOTRITON) and discuss the choice of configuration parameters in Sect. 3. Illustrative examples are given in Sect. 4, and a comparison of the CALOTRITON UHF-based Z_i estimates to in situ measurements is presented in Sect. 5. A conclusive discussion is presented in Sect. 6.

2 Instrumentation and data

2.1 Datasets

In this study, we consider the data of the LAERO UHF RWP at P2OA-CRA from 2015 to 2022 to develop the new CALOTRITON algorithm. This time period is shorter than the whole available time series for the sake of data process homogeneity. The year 2018 is more intensively used for the primary development of the algorithm. We also use sensible heat flux measurements from a sonic anemometer installed at 30 m on the P2OA-CRA 60 m instrumented tower and relative humidity measurements made at 2 m.

To optimize CALOTRITON parameters, we compare Z_i estimates with cloud base heights (Sect. 3.3) measured by a CT25k ceilometer from Centre National de Recherche Météorologique (CNRM) present from December 2016 to December 2019 at P2OA-CRA.

The algorithm results are then validated (see Sect. 5) by comparison to in situ profiles made using a radiosonde or remotely piloted aircraft system (RPAS) during two intensive field campaigns; (i) BLLAST (Boundary-Layer Late Afternoon and Sunset Turbulence; Lothon et al., 2014), which took place at P2OA-CRA, and (ii) LIAISE (Land surface Interactions with the Atmosphere over the Iberian Semi-arid Environment; Boone et al., 2021), which took place in northeast Spain, close to Lleida. The latter enables us to test CALOTRITON in a meteorological and geographical context other than that of the long-term observational record of P2OA-CRA and thus generalize its applicability and use. For both measurement campaigns, the CNRM UHF RWP is used in addition to the LAERO UHF RWP, which also enables testing the algorithm on a different UHF RWP.

Table 1 summarizes the contexts of RWP measurements used and corresponding time periods, the location of RWPs, the complementary instrumentation used, and their role in this study. The corresponding datasets are listed and referenced in the "Data availability" section at the end of the article, with more precision on the specific periods for each instrument.

The sensible heat flux is calculated using 30 min duration samples with EddyPro software, based on the eddy correlation technique. The UHF RWP instruments and data process are detailed in the following section.

2.2 UHF radar wind profiler technical characteristics and data process

The LAERO UHF RWP is a 1.274 GHz wind profiler with five beams, four oblique beams, and one vertical beam. Its main characteristics are listed in Table 2 (for more details, see Jacoby-Koaly, 2000). It alternates between two modes: a "low mode" with a pulse width of 500 ns corresponding to a range resolution of 75 m and a "high mode" with the pulse width of 2.5 µs corresponding to a range resolution of 150 m and a slightly better height coverage. For our use here, we only consider the low mode. The maximum height for this mode is usually around 3000 m a.g.l. but may be only 500 or 1000 m in winter, when dry anticyclonic conditions occur. It can reach 7 or 9 km within deeper clouds and rain. The first gate is at 75 m but with a poor confidence index. We consider the 225 m gate to be the first gate with very good confidence. The CNRM UHF RWP mainly presents the same characteristics but with the first level with a good confidence index at 300 m.

The three components of the wind are deduced from the Doppler radial velocity of the five beams every 75 m and every 2 min. The first main critical step is to select the meteorological peak from the Doppler spectrum. We use a process developed at the LAERO laboratory, which optimizes the meteorological peak selection and data coverage relative to the manufacturer processing. During this phase, an automatic quality control is done, eliminating Doppler spec-

Table 1. Summary of instruments used and context.

Context	Period	RWP	RWP location	Complementary instrumentation	Use for CALOTRITON
P2OA	2015–2022	LAERO UHF RWP	Campistrous, France	Sonic anemometer CSAT3 Humidity sensor HMP45 CT25k ceilometer Radiosoundings	optional input input configuration optimization validation
BLLAST	June–July 2011	LAERO UHF RWP	Campistrous, France	Sonic anemometer CSAT3 RPAS Radiosoundings	optional input validation validation
		CNRM UHF RWP	Capvern, France	RPAS Radiosoundings	validation validation
LIAISE	July 2021	LAERO UHF RWP	Els Plans, Spain	Sonic anemometer Radiosoundings	optional input validation
		CNRM UHF RWP	La Cendrosa, Spain	Sonic anemometer Radiosoundings	optional input validation

Table 2. Main characteristics of the Laboratoire d'Aérologie's ultra-high-frequency radar wind profiler (LAERO UHF RWP; https://p2oa.aeris-data.fr/sedoo_instruments/profileur-de-vent-uhf/, last access: 22 March 2024).

Manufacturer	Degreane
Reference	PCL1300
Emission frequency	1.274 GHz
Number of beams	5 (N, W, S, E, and vertical)
Transmission frequency	1274 MHz
Opening angle	8.5°
Oblique antenna angle	17° to the vertical
Vertical resolution	75 m
Temporal resolution	∼ 2 min
First level with a good confidence index	225 m
Vertical coverage	∼ 3 km

tral erroneous peaks before the wind component calculation. The second step is typical of the velocity volume processing technique (Wadteufel and Corbin, 1979), which computes the three wind components from the radial velocity with a minimum least-squares error. The air refractive index structure coefficient C_n^2 is deduced from the reflectivity as a function of the received power (Doviak and Zrnic, 1993). The vertical velocity variance σ_w^2 is obtained from the Doppler spectral half-width of the backscattered signal on the vertical beam and gives and allows for the estimation of TKE dissipation rate ε (Cohn and Angevine, 2000; Jacoby-Koaly et al., 2002). Hereafter, C_n^2 is the median air refractive index structure coefficient over the five beams and depends on altitude and time. ε is the median TKE dissipation rate over the five beams. σ_w is deduced from the vertical antenna and corrected for the effect of the horizontal wind within the antenna aperture (Jacoby-Koaly et al., 2002). All those variables are calculated at 2 min time intervals.

3 The CALOTRITON algorithm

3.1 CALOTRITON specific objectives

The new Z_i-retrieval algorithm (CALOTRITON) was developed with five main objectives and constraints in mind:

1. to restrict the Z_i estimate to the convective boundary layer by only considering daytime conditions and excluding precipitation periods;

2. to respect the temporal continuity of Z_i growth and to follow it as finely as possible in time in order to describe the smallest convective scales (5 to 30 min; Stull, 1988), as Z_i should start close to the ground early in the day;

3. to manage complex cases, as in the presence of clouds or thermal internal boundary layer (TIBL) or when cold air advection in the lower layers can create a new convective boundary layer such as in the case of slope wind (Kossmann et al., 1998) or sea breeze (Durand et al., 1989);

4. to take into account abrupt CBL growth, which occurs in the presence of a residual neutral layer above Z_i, when the current CBL potential temperature gets to reach the residual neutral layer potential temperature (Blay-Carreras et al., 2014);

5. to use limited instrumental synergy in order to apply it in other sites (or measurement campaigns) equipped with a UHF RWP and not to depend on the availability of an advanced instrument suite to establish the Z_i estimate.

3.2 CALOTRITON operation

Figure 2 presents a scheme of the CALOTRITON algorithm, which is described in this section, and Table 3 recapitulates

the variables used at the different steps of CALOTRITON with the corresponding timescales.

3.2.1 Restriction to CBL conditions

First, we consider UHF RWP data only above 225 m a.g.l. and below 3000 m a.g.l. The height of 225 m is the first gate where data are always of high quality. Only daytime data are selected to estimate Z_i from the UHF RWP. For this, sunrise and sunset times are retrieved as a function of date, altitude, latitude, and longitude. Precipitation periods (including virga) are excluded by a function based on empirical thresholds on C_n^2 and Doppler vertical velocity (w). Any profile which meets $C_n^2 > 10^{-14}$ m$^{-2/3}$ and $w < -1$ m s^{-1} over five consecutive levels is removed, including all profiles occurring 15 min before and after. We do not assign Z_i in the case of fogs, notably due to the limitation of the UHF RWP below 225 m a.g.l. It was found at the P2OA site that relative humidity at 2 m larger than 90 % was associated with fog occurrence as confirmed by ceilometer measurements (not shown). We therefore take this as a criterion for fog occurrence and remove corresponding periods from the further analysis.

3.2.2 Data averaging

In order to disregard non-meteorological disturbances (e.g. birds) affecting the UHF RWP signal, C_n^2, σ_w, and ε data are filtered by complementary sliding median filters:

- C_n^2 and ε – a median over 6 min (three data points), none over the height in order to keep the original UHF RWP vertical resolution of 75 m;

- σ_w – a median over 8 min (four data points) and a median over 225 m (three points) because of a more pronounced spatiotemporal variability in these data (see Figs. 4d, 6d, 8d), using coarser filters for σ_w to compensate for the fact that C_n^2 and ε are already integrated over the five beams.

If a larger integrated time is chosen, the corresponding median time filter should be adjusted and applied to C_n^2, ε, and σ_w.

3.2.3 Definition of intermediate key variables

As the reflectivity maximum does not always correspond to Z_i, especially in the case of a cloudy sky, we suggest using a new dimensionless variable which takes into account both the increase in reflectivity at the summital inversion and the decrease in turbulence; the variable NPx (Eq. 1) weighs C_n^2 by σ_w to the power of x and allows for a better account of a large value of C_n^2 associated with a small value of σ_w. Dimensionless NPx is obtained by averaging values of C_n^2 and σ_w^x up to 3000 m for each profile (overlines in Eq. 1):

$$\mathrm{NP}x = \frac{C_n^2 / \overline{(C_n^2)}}{\sigma_w^x / \overline{\sigma_w^x}}. \tag{1}$$

Dimensionless NPx is computed with the filtered data discussed previously (Sect. 3.2.2) and is linearly integrated over a 5 min time step to describe the smallest characteristic convective scale. The choice of x is discussed in Sect. 3.3.2. As an example, Figs. 4d and 6d discussed later show cross sections of NP3 in a simple and complex case respectively. Note that this approach is based on the same main assumption as in the methods proposed by Heo et al. (2003) and Bianco and Wilczak (2002), who also combined the need for an increase in reflectivity and a decrease in turbulence.

We also consider another variable purely defined by the level of turbulence; variable Z_{i_ε} is the height above the surface at which the TKE dissipation rate ε falls below 5×10^{-4} m^2 s^{-3}. This technique was previously used by Couvreux et al. (2016) and Nilsson et al. (2016a). It thus represents a rough estimate of the depth of significant turbulence. Height Z_{i_ε} is computed on filtered and integrated ε data (5 min as NPx). In order to consider only the Z_{i_ε} that would respect a certain temporal continuity, a sliding median filter over 15 min (three points) is applied to Z_{i_ε}.

Variable NPx is the core variable of CALOTRITON, but Z_{i_ε} will help us with documenting the associated turbulence and optimize the selection of the most appropriate local maximum of NPx as an estimate of Z_i (we hereafter call this selection "Z_i attribution").

3.2.4 Determination of the first Z_i estimate of the day

In a typical CBL development, Z_i starts close to the ground, below the UHF RWP detection limits (225 m), and grows until it reaches a plateau in the early afternoon (Stull, 1988). It is therefore necessary to wait for some time (called t_{init}) before Z_i can be detected by the UHF RWP. We found that the sensible heat flux, which governs the evolution of Z_i, remains very low (lower than a few tens of W) at least until 1.5 h after sunrise (not shown). Therefore, t_{init} is not defined before 1.5 h has passed after sunrise.

Several methods are used to determine t_{init}. The first is based on C_n^2 at the first reliable UHF RWP gate (225 m a.g.l.) and considers t_{init} to be the time when the 30 min sliding median exceeds its daily mean value. That way, it is investigated when an increase in C_n^2 becomes significant and may correspond to Z_i. The second method is based on the measured sensible heat flux (H) and considers t_{init} when H exceeds the significant threshold of 50 W m^{-2}. In that case, t_{init} is taken as the earliest time over those two. The first assigned Z_i of the day ($Z_i(i=0)$) can only be established at a local maximum of the vertical profile of NPx located at one of the two first reliable levels of the UHF RWP and occurring after t_{init}.

Sometimes, a thin layer is mixed by dynamical turbulence before sunrise, e.g. in the presence of a low-level jet. In order to take those situations into account, we allow the attribution of the first Z_i at the height of Z_{i_ε} if the latter corresponds exactly to the height of the NPx maximum of the profile inde-
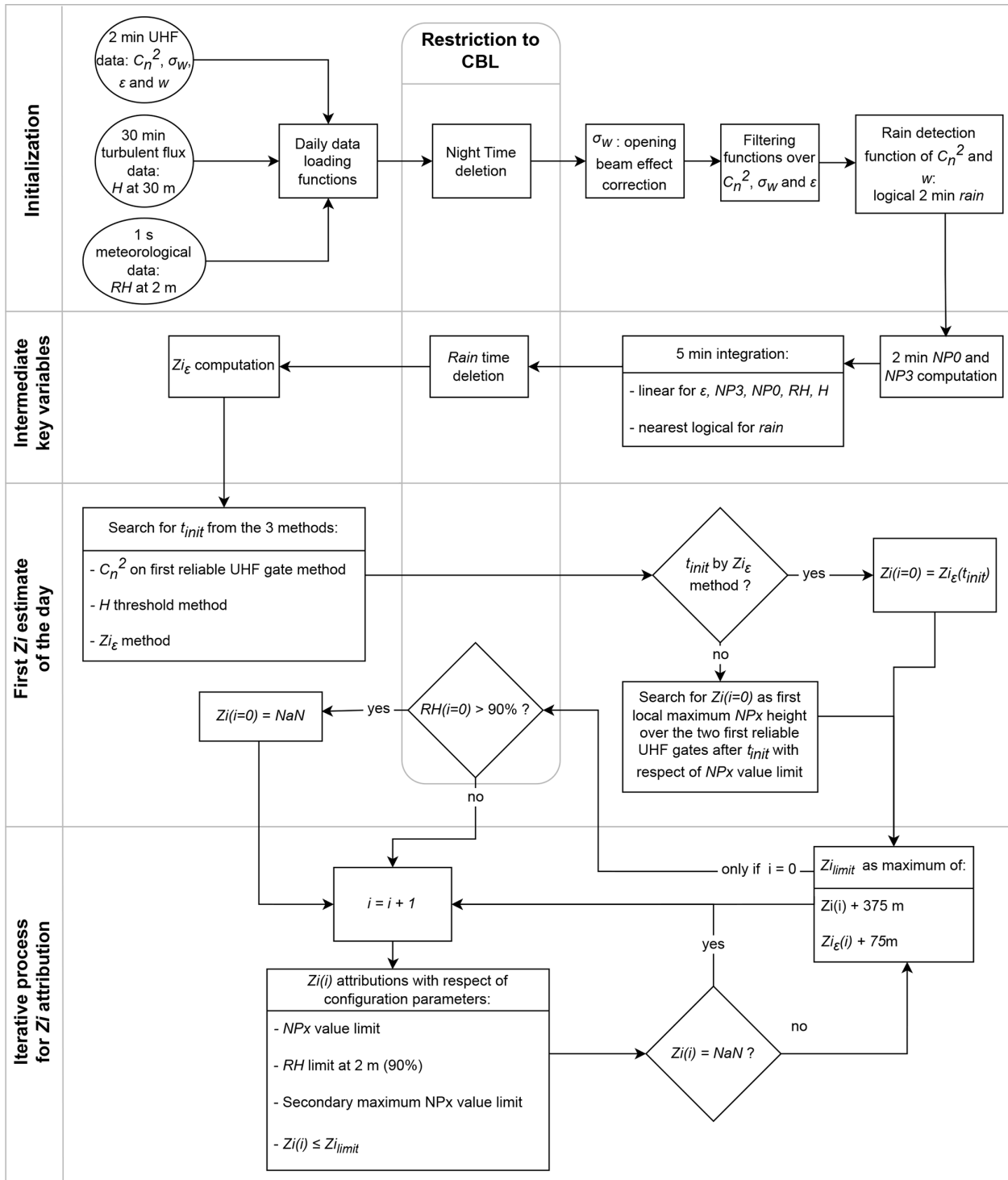
Figure 2. CALOTRITON organization chart.

pendently of t_{init} and provided that this attribution is always done 1.5 h after sunrise.

This initialization process is somehow similar to Molod et al. (2015), who called this time the "emergence time" and determined it based on the same principle; i.e. they also con-

sider a first good-confidence gate and look for the first determinable Z_i at this level but in a different way.

Table 3. Variables used in CALOTRITON at the different steps of the algorithm and their time intervals.

Input variables	C_n^2, σ_w, ε, and w	2 min	Main input variables
	H	30 min	t_{init} assessment (optional)
	RH	1 s	Fog occurrence estimation (optional)
Filtered variables	C_n^2, σ_w, and ε	5 min	
Calculated variables	NPx and Z_{i_ε}	5 min	Key intermediate variables
	t_{init}	1 d	Key CBL growth starting variables
Auxiliary variable	CBH	1 min	Configuration optimization
Final variables	$Z_{i_{NP3_{std}}}$	5 min	Best estimate
	$Z_{i_{NP0_{std}}}$, $Z_{i_{NP0_{sup}}}$, and $Z_{i_{NP0_{sub}}}$	5 min	Complementary estimates
	QF	5 min	Quality assessment

3.2.5 Iterative process for Z_i attribution

Once the initial Z_i is found, the search for subsequent Z_i is done by temporal iteration on the most significant local maximum of NPx that is located within a vertical growth limit of 375 m since its last effective attribution. Residual layers or clouds above Z_i can potentially return a higher signal contribution to NPx than Z_i itself and might be misinterpreted if located within the 375 m growth limit. To take this into account, the algorithm allows for attributions to local secondary maxima of NPx below the first maximum value if the value of the corresponding NPx is at least 90 % of the first maximum value of NPx before 10:00 UTC and 50 % after. These empirical values are discussed in Sect. 3.3.2 and named relative thresholds of the secondary maximum of NPx. Finally, a minimum value of NPx is required for attribution and fixed to the mean profile value of NPx in order to take into account a certain significance. Sometimes, strong growth of Z_i can occur and exceed the imposed limit (375 m). This motivated us to use Z_{i_ε} in order to consider up to which level significant turbulence is found. If at i time $Z_{i_\varepsilon}(i)$ is higher than the last effective attribution plus the growth limit, then $Z_i(i)$ can be searched up to $Z_{i_\varepsilon}(i) + \mathrm{d}z$ (where $\mathrm{d}z = 75$ m).

3.3 Algorithm parameter choice

3.3.1 Parameter optimization

All the parameters presented above were obtained empirically by subjectively judging the quality of the attributions of Z_i for about 100 d in 2018 at P2OA-CRA. In order to verify their quality in a more objective way and possibly to adjust some parameters, we compared the estimates of Z_i with the lowest cloud base height (CBH) measured by the CT25k ceilometer within a 5 min interval of each attribution. This comparison is based on data from December 2016 to December 2019. When comparing the two configurations with the distributions shown in Fig. 3, one would favour the con-

figuration which leads to fewer attributions above cloud base and lower values of ε at Z_i.

Figure 3 shows an example of the results of this comparison for Z_i estimates based on either NP3 or NP0, with the use of the optimal parameters listed in Table 4. Figure 3a shows the distribution of the set of Z_i attributions for the different values of NPx ($x = 0$ and $x = 3$) and indicates more attributions by NP3, especially for $Z_i < 700$ m. Figure 3b shows the distribution of the differences between Z_i and CBH. It can be seen that there are slightly more attributions above the cloud base when using NP0. Figure 3c presents the distribution of all ε values at Z_i height and shows that NP3 attributions tend to get lower ε values at Z_i height. The fact that NP3 attributions of Z_i are more often lower than NP0 attributions and associated with lower ε values is a sign of better quality attributions. When clouds are present, the difference between Z_i estimates based on NP3 and NP0 is on average twice as large as in clear-sky cases due to the complexity of the atmosphere in cloudy conditions. Thus, the observed differences between Z_i attributions based on NP3 and NP0 give an indication of the CBL complexity. Figure 3d–f present the same figure as the top panels (Fig. 3a–c) but only considering the attributions by NP3 and NP0 when they differ by more than 225 m from each other. This represents only 10 % of the total attributions. The same conclusions as previously stated can be drawn even more clearly here. We therefore confirm that NP3 statistically gives better results.

3.3.2 Tested parameters and optimum set

In this way, the set of NPx values for $x = 1$ to $x = 5$ was compared two by two with the configuration presented in Table 4. It was noted that attributions were potentially better for $x = 3$ than $x = 0$, 1, or 2. However, no significant trend was noticed for $x \geq 3$. We limit ourselves to $x = 3$ in order to keep the attributions predominantly based on C_n^2. In this section, only a few results of our search for the best parameters by attribution distribution analysis are presented. All are based on NP3. The largest differences appeared between
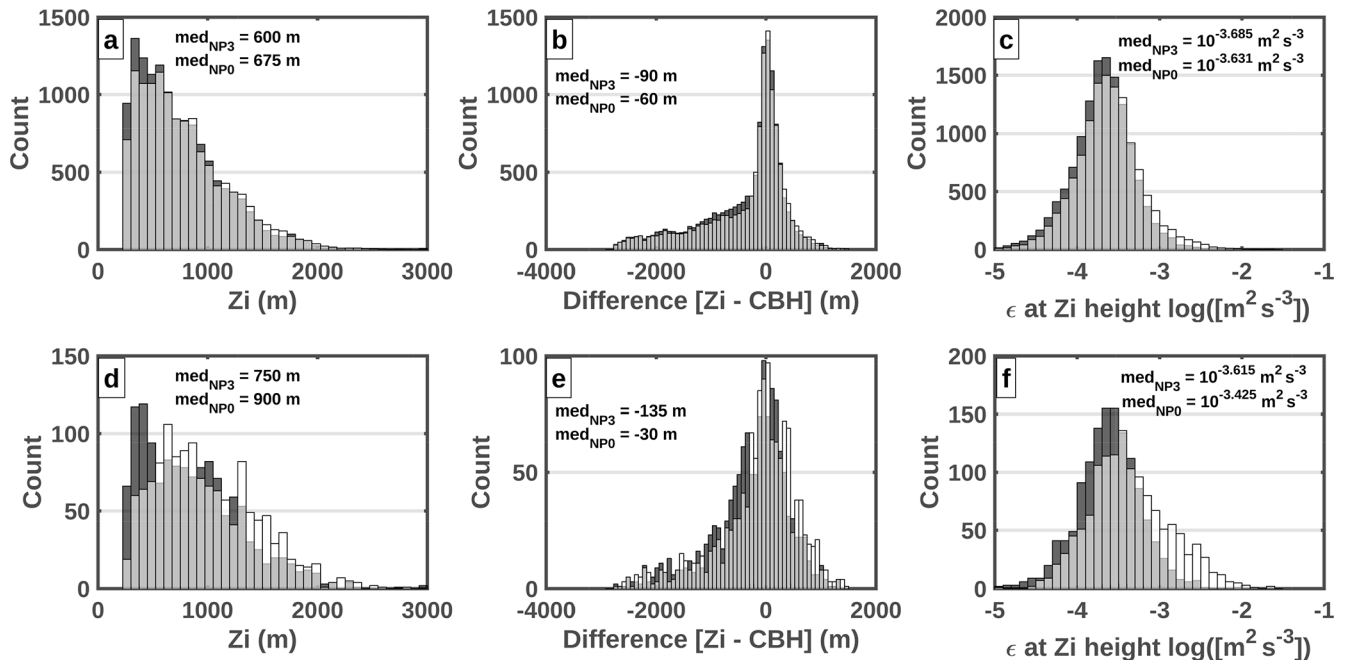
Figure 3. Histograms showing the differences between the distributions of $Z_{i_{NP0_{std}}}$ (white bar) and $Z_{i_{NP3_{std}}}$ (black bar) in the presence of clouds measured by the CT25k ceilometer from December 2016 to December 2019: **(a)** Z_i distribution, **(b)** distribution of difference between Z_i and cloud base height, and **(c)** ε-value distribution at Z_i height. Panels **(d)** to **(f)** are respectively the same as panels **(a)** to **(c)** but considering only attributions which present more than 225 m difference between $Z_{i_{NP0_{std}}}$ and $Z_{i_{NP3_{std}}}$. For the distributions of $Z_{i_{NP3_{std}}}$ and $Z_{i_{NP0_{std}}}$, the median values are indicated by med$_{NP3}$ and med$_{NP0}$ respectively.

Table 4. List of the best parameters for CALOTRITON configuration.

Criterion number	Parameter	Value	Comments
1	Integration time	5 min	
2	Time median filter C_n^2	Three points	~ 6 min
3	Time median filter ε	Three points	~ 6 min
4	Time median filter σ_w	Four points	~ 8 min
5	Height median filter C_n^2	Zero points	0 m
6	Height median filter ε	Zero points	0 m
7	Height median filter σ_w	Three points	225 m
8	Growth limit	375 m	between two effective assignments
9	Relative humidity limit at 2 m	90 %	
10	NPx value limits	NPx profile mean	
11	Secondary maximum NPx value limit	90 % before and 50 % after 10:00 UTC	criterion no. 10 applied
12	Z_{i_ε} option	True	to exceed the growth limit

whether or not we considered a limit on relative humidity. Not setting a limit allows for about 4 % more attributions in clear-sky conditions and 40 % more in the presence of clouds. Among those 40 %, half of them correspond to cloud base heights below 225 m, which is the first level of the UHF RWP. Considering the limit on relative humidity, 13 % of all attributions in the presence of clouds take place 225 m above the cloud base compared to 22 % without a limit. This limit,

therefore, both avoids attributions in the presence of clouds whose base is below the UHF RWP lower limit and reduces the number of attributions above the cloud base by half.

The methods for the search for t_{init} were tested. Using solely the C_n^2 maximum technique leads to almost no difference in Z_i attributions, but, additionally, using the technique based on sensible heat flux leads to 3 % more attributions.

Other values related to the growth limit were also tested. It was noticed that a limit of 300 m with the last effective attribution potentially allows for better quality attributions to be obtained but leads to a reduction of 3 % in the attributions compared to a limit of 375 m. Empirically, it was found that 300 m was not sufficient to properly track the evolution of Z_i compared to 375 m. On the other hand, a 450 m growth threshold did not improve the results statistically. Although it leads to an increase in the total number of attributions by 3 %, all additional attributions under cloudy skies were above the cloud base. This is the reason we finally chose 375 m as the optimal growth threshold.

Other important parameters are the values selected for the relative thresholds of secondary maximum NPx on which attributions are possible. Not setting a limit leads to an increase of 40 % in attributions above CBH + 225 m, which is associated with higher ε values and thus less appropriate. Thresholds of 50 % and 90 % were tested over the whole day, and it was found that the threshold of 50 % led to more attributions over residual layers than the threshold of 90 %, especially in the morning. In contrast, a threshold of 90 % leads to more attributions inside the CBL, especially in the afternoon. This is why thresholds of 90 % before 10:00 UTC and of 50 % afterwards were chosen. A threshold of 75 % for the whole day was also tested but provided poorer results.

3.3.3 Final assignment and flags

As we have seen previously, the difference between NP0 and NP3 attributions with the parameter set as described in Table 4 gives useful and complementary information about the complexity of the lower troposphere. This is why we perform the following four estimates of Z_i:

– $Z_{i_{\mathrm{NP3_{std}}}}$ is estimated with the standard configuration for NP3 as described in Table 4, which is considered to be the best set of attributions.

– $Z_{i_{\mathrm{NP0_{std}}}}$ is estimated with the standard configuration for NP0 as described in Table 4.

– $Z_{i_{\mathrm{NP0_{sup}}}}$ is estimated from NP0 as described in Table 4 but without applying criteria nos. 9, 10, and 11. With this configuration, the 375 m growth limit (no. 8) is applied between the Z_i searched for and the already allocated maximum Z_i. There is also no t_{init} restriction after sunrise. This configuration allows for the search for levels higher than the estimates made with a standard configuration, which may correspond to the top of a residual layer or to Z_i if the standard configuration assigns it to a TIBL top.

– $Z_{i_{\mathrm{NP3_{sub}}}}$ is estimated from NP3 as described in Table 4 but without applying criterion no. 11. With this configuration, the NPx profile mean of the criterion no. 10 is replaced by the median, which gives lower values most of the time, mainly because of high values of C_n^2. This

configuration allows us to search for levels lower than the estimates made with a standard configuration, which may correspond to a TIBL top or to Z_i if the standard configuration assigns it to a residual layer top.

Our best proposed estimate is $Z_{i_{\mathrm{NP3_{std}}}}$ for the reasons explained earlier. However, the four estimates embed the large complexity that is often observed in the lower troposphere.

In order to qualify this complexity and to facilitate the correct use of the four estimates, a quality flag QF is defined as follows:

– When QF = 1, all attributions are equal. It indicates very good confidence in the assignment quality and a textbook case.

– When QF = 2, only $Z_{i_{\mathrm{NP3_{std}}}}$, $Z_{i_{\mathrm{NP0_{std}}}}$, and $Z_{i_{\mathrm{NP3_{sub}}}}$ are equal. It indicates good confidence in the assignment quality and the likely presence of a residual layer above Z_i located at $Z_{i_{\mathrm{NP0_{sup}}}}$. It also indicates that the Z_i estimate does not match the height of the C_n^2 maximum.

– When QF = 3, only $Z_{i_{\mathrm{NP3_{std}}}}$, $Z_{i_{\mathrm{NP0_{std}}}}$, and $Z_{i_{\mathrm{NP0_{sup}}}}$ are equal. It indicates medium confidence in the assignment quality and the likely presence of a TIBL located at $Z_{i_{\mathrm{NP3_{sub}}}}$.

– When QF = 4, only $Z_{i_{\mathrm{NP3_{std}}}}$ and $Z_{i_{\mathrm{NP0_{std}}}}$ are in exact agreement. It indicates medium confidence in the assignment quality and the likely presence of both a TIBL and a residual layer located at $Z_{i_{\mathrm{NP3_{sub}}}}$ and $Z_{i_{\mathrm{NP0_{sup}}}}$ respectively.

– When Q = 5, there is no agreement between the four attributions of heights. This indicates poor confidence in the assignment quality and a highly complex case.

Other flags could be produced in order to more thoroughly document the meaning of those various estimates. They could, for example, qualify the temporal continuity of $Z_{i_{\mathrm{NP3_{std}}}}$ (i.e. the occurrence of abrupt changes) or the consistency of $Z_{i_{\mathrm{NP3_{std}}}}$ with Z_{i_ε}.

4   Illustrative case studies

In this section, we present three study cases to illustrate the capability of CALOTRITON and the improvements of Z_i retrieval relatively to a more standard approach:

– a reference simple clear-sky case (27 October 2021 at P2OA),

– a complex cloudy-sky case (15 March 2018 at P2OA),

– a complex multiple-layering clear-sky case (27 July 2021 during the LIAISE field experiment).
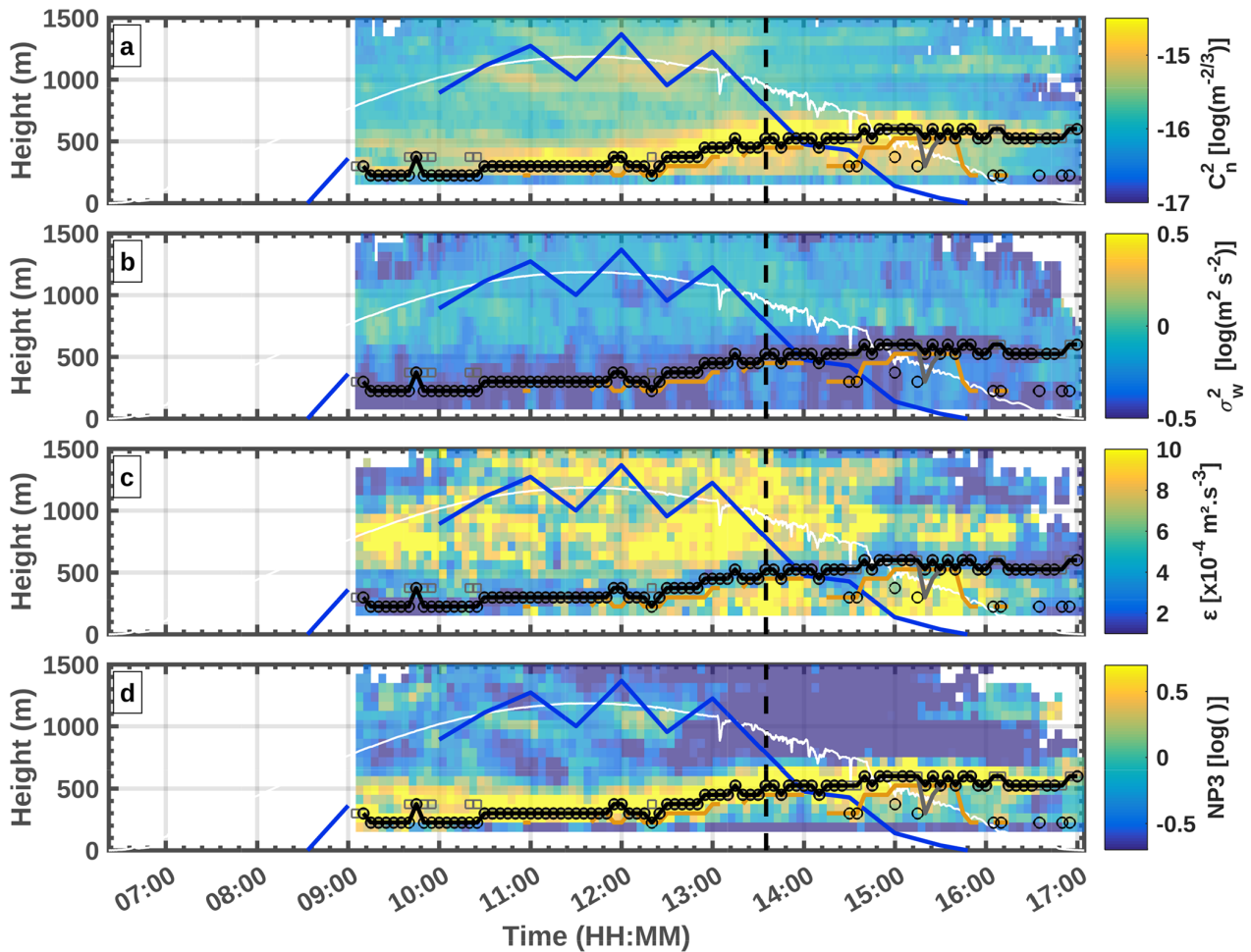
Figure 4. UHF RWP observations for 27 October 2021 at P2OA-CRA during clear-sky conditions: **(a)** filtered C_n^2 in log scale, **(b)** filtered σ_w^2 in log scale, **(c)** filtered and integrated ε in log scale, and **(d)** integrated NP3 in log scale. For all panels, Z_i estimates are as described in Sect. 3.2.2 and 3.3.3 – Z_{i_ε} (orange line), $Z_{i_{\mathrm{NP0_{std}}}}$ (grey line), $Z_{i_{\mathrm{NP0_{sup}}}}$ (grey squares), $Z_{i_{\mathrm{NP3_{std}}}}$ (black line), and $Z_{i_{\mathrm{NP3_{sub}}}}$ (black circles) – and based on the same ordinate axis (but with different units), i.e. downward shortwave radiation (W m^{-2}) (white line) and sensible heat flux (dW m^{-2}) (thick blue line). The vertical dashed line corresponds to the time of the discussed radiosounding.

4.1 Clear-sky case at P2OA

Figure 4 shows the height–time section of four UHF-based variables defined earlier: the air refractive index structure coefficient C_n^2 (Fig. 4a), the air vertical velocity variance σ_w^2 (Fig. 4b), the turbulence kinetic energy (TKE) dissipation rate ε (Fig. 4c), and the new combined parameter NP3 (Fig. 4d).

The downward shortwave radiation (white line) and the sensible heat flux (blue line) are overlaid on all panels. The shortwave radiation shows that this day was mainly clear with only a few thin and occasional cirrus clouds in the afternoon. Sensible heat flux shows a typical diurnal cycle. Also overlaid are different estimates of Z_i defined in the previous section ($Z_{i_{\mathrm{NP0_{std}}}}$, $Z_{i_{\mathrm{NP0_{sup}}}}$, $Z_{i_{\mathrm{NP3_{std}}}}$, and $Z_{i_{\mathrm{NP3_{sub}}}}$) and the intermediate variable Z_{i_ε}. We note for this case very large consistency between the four different estimates $Z_{i_{\mathrm{NP}x}}$. That

means whatever the method, standard or more sophisticated, taking account of turbulence intensity or not, they all agree for the Z_i estimation for the CBL growth and simply match the absolute maximum reflectivity for most of the time.

In order to make the correspondence between the UHF RWP and the thermodynamical profiles, Fig. 5 compares in situ measurements of thermodynamical variables measured by radiosondes with the UHF RWP measured variables at 13:35 UTC on this same clear day of 27 October 2021.

The comparison shows that the absolute maximum reflectivity corresponds well to the CBL top, characterized by a strong gradient of the potential temperature and mixing ratio (Fig. 5a and b). It also shows that σ_w^2 (Fig. 5e) and ε (Fig. 5f) are small at this height, leading to a local minimum. On "ideal" clear days without external forcing, we would typically not observe significant turbulence above Z_i (Fig. 1e). In this case, forcing is small with weak wind, but
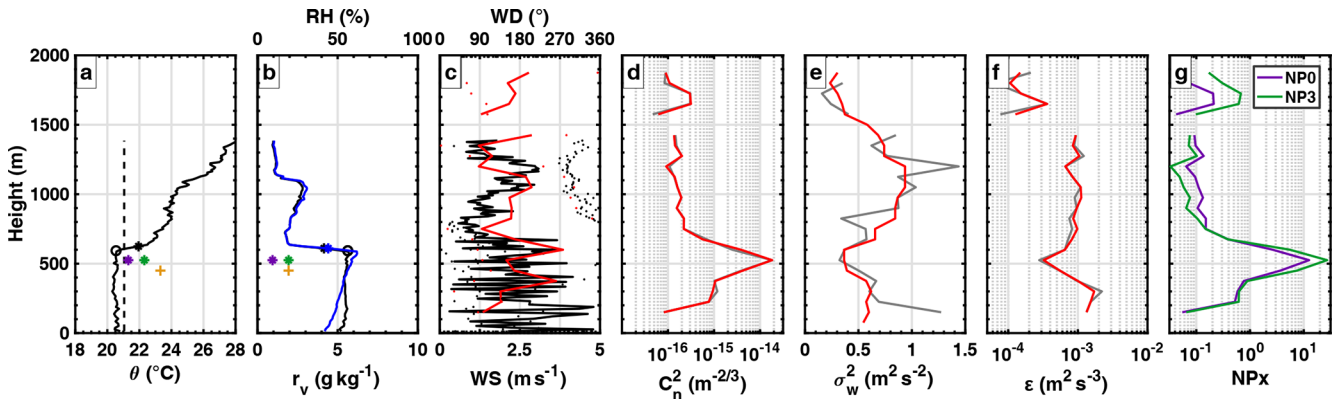
Figure 5. Profiles measured by radiosondes and UHF RWP at P2OA-CRA on 27 October 2021 at 13:35 UTC. **(a)** Potential temperature (solid black line), surface potential temperature $+0.25\,°C$ (dashed black line), Z_i from the in situ subjective method (black circle), Z_i from the in situ potential temperature gradient method (black asterisk), $Z_{i_{NP0_{std}}}$ (purple "×"), $Z_{i_{NP0_{sup}}}$ (purple "+"), $Z_{i_{NP3_{std}}}$ (green "×"), $Z_{i_{NP3_{sub}}}$ (green "+"), and Z_{i_ε} (orange "+"). **(b)** Mixing ratio (black line) and relative humidity (blue line), Z_i from the in situ mixing ratio gradient method (black asterisk), Z_i from the in situ relative humidity gradient method (blue asterisk); purple, green, and orange crosses denote the same values as described in panel **(a)**. **(c)** Wind speed (solid line) and wind direction (dotted line) from the radiosonde (black) and UHF RWP (red). **(d)** Air refractive index structure coefficient from UHF RWP with raw data (grey line) and filtered data as described in Sect. 3.2.2 (red line). **(e)** Vertical velocity variance from UHF RWP with the same colour scheme as in panel **(d)**. **(f)** TKE dissipation rate from UHF RWP with the same colour scheme as in panel **(d)**. **(g)** NP0 (purple line) and NP3 (green line).

the wind shears still generate significant turbulence (Fig. 4c). In a subjective way, we estimate Z_i at about 550 m from this radiosonde, where a strong potential temperature gradient is observed, which is associated with a strong humidity gradient (mixing ratio and relative humidity). This height is in good agreement with all the estimates made by CALOTRITON at that time and with the simplest standard estimate of Z_i made by RWP. This case is a typical clear-sky case with QF = 1 for most of the day (Fig. 4). Height $Z_{i_{NP3_{std}}}$ consequently has a good confidence index, except around 15:30 UTC, where $Z_{i_{NP0_{std}}}$ is slightly lower than $Z_{i_{NP3_{std}}}$. Note in Fig. 4 that Z_{i_ε} remains equal to or below those estimates and especially decreases in the late afternoon with a strong decay of the surface flux. This is one typical late afternoon transition scenario, as described in Grimsdell and Angevine (2002) and Lothon et al. (2014). Value $Z_{i_{NP3_{sub}}}$ also interestingly decays during the same phase, thus defining a potential pre-residual layer situated between $Z_{i_{NP3_{sub}}}$ (or Z_{i_ε}) and $Z_{i_{NP3_{sup}}}$ (or $Z_{i_{NP3_{std}}}$). The pre-residual layer is defined when the surface heat flux is not strong enough anymore to keep the mixing up to the midday summital inversion and falls between the thinning turbulence layer and the residual inversion (Nilsson et al., 2016b; Lothon et al., 2024). The different estimates made in CALOTRITON can thus help identify interfaces and layers in the complex afternoon transition phase. Standard and simple methods do not enable us to describe this subtle and still poorly understood complexity.

4.2 Complex cloudy case at P2OA

Figure 6 gives another example of UHF RWP measurements on 15 March 2018, this time with a marked external forcing, identified by a cloudy sky and high wind speed in the upper layer. For this figure, the cloud base height measured with the ceilometer is added and also revealed by the downward shortwave radiation.

In this complex case, the maximum of C_n^2 remains constant for most of the day between 2000 and 3000 m, related to the clouds and associated hydrometeors rather than to the top of the CBL. This makes $Z_{i_{NP0_{sup}}}$ high in this nearby cloud layer. Between 10:00 and 11:30 UTC, this maximum of C_n^2 is competitive with the local maximum below, which is what we can interpret as the top of the growing CBL and which is better detected with NP3. Between 16:00 and 17:20 UTC, the reflectivity field shows the presence of virga (verified by observations of the weather radars of Météo-France). In cases where droplet size is close to the RWP wavelength, this induces a strong reflectivity (and C_n^2) on the entirety of the profiles. For this more complex case, $Z_{i_{NP0_{std}}}$, $Z_{i_{NP3_{std}}}$, and $Z_{i_{NP3_{sub}}}$ are consistent only until 11:00 UTC. After this time, $Z_{i_{NP0_{std}}}$ and $Z_{i_{NP0_{sup}}}$ are higher than $Z_{i_{NP3_{std}}}$ and $Z_{i_{NP3_{sub}}}$, suggesting that the latter may be assigned to the top of a TIBL. After 11:30 UTC, the assignments based on NP3 become more discontinuous due to the limit of NPx values (NPx profile mean). This discontinuity indicates an increased uncertainty in the attributions. Value $Z_{i_{NP0_{sup}}}$ is then systematically located above the others, suggesting that $Z_{i_{NP3_{std}}}$ may potentially identify the top of a TIBL. However, we believe that these attributions are correct as they are located at the
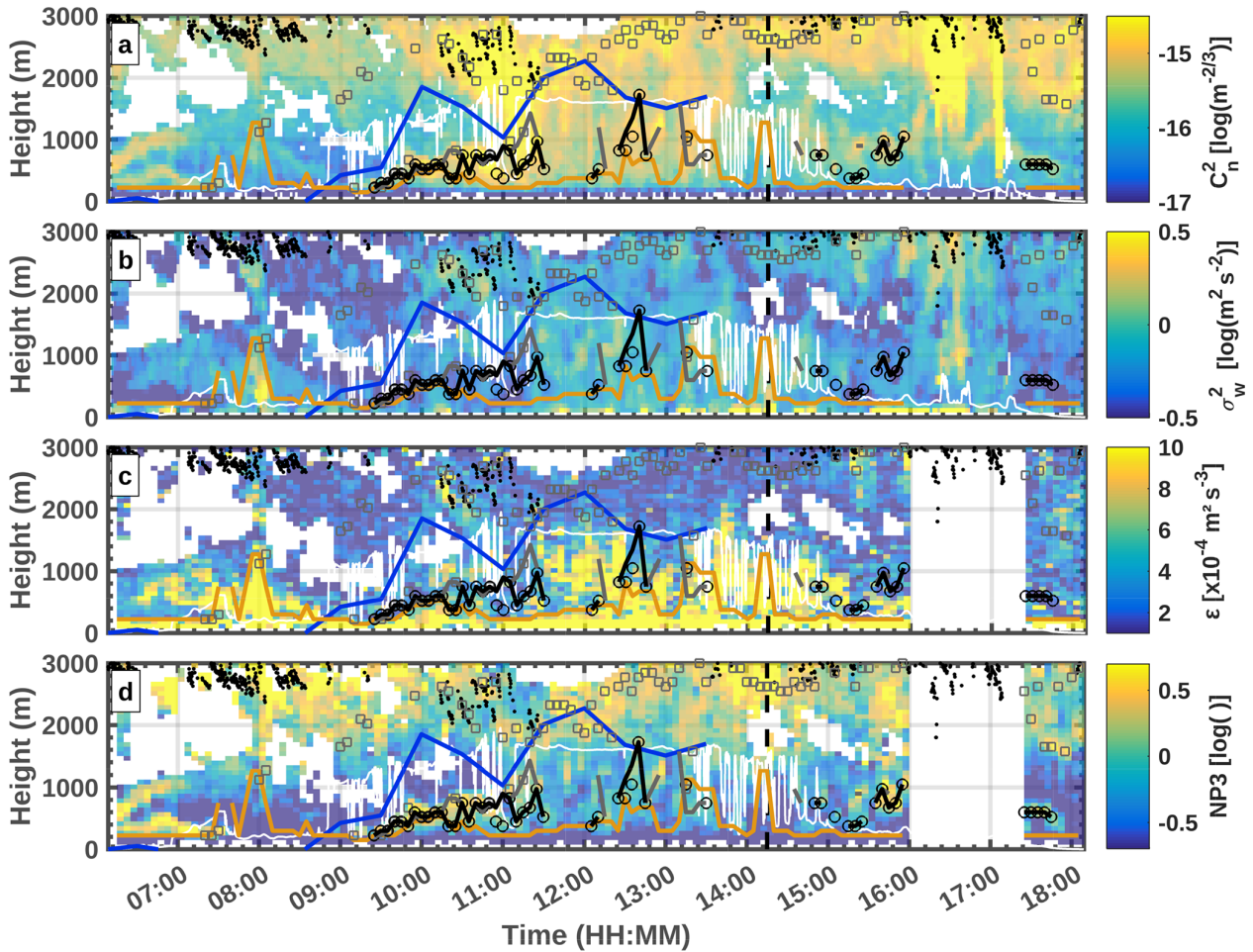
Figure 6. LAERO UHF RWP observations for 15 March 2018 at P2OA-CRA with the same description as Fig. 4 and cloud base height measured by the CT25k ceilometer (black dots).

height where the strongest wind shear is observed. After 15:00 UTC, Fig. 6 shows more discontinuity on $Z_{i_{NP3_{std}}}$ attributions, demonstrating a CBL complexity with small incoming shortwave radiation, no positive sensible heat flux, and the occurrence of precipitation mentioned above.

In order to better interpret this complex day, Fig. 7 compares in situ measurements of thermodynamical variables with the UHF RWP variables at 14:15 UTC on that same day.

In a subjective way, Z_i can be estimated at 1500 m from this radiosounding (Fig. 7a), the height where the atmosphere starts to be stable (positive θ gradient), which is also associated with a strong discontinuity in the mixing ratio profile. This height corresponds well to $Z_{i_{NP3_{std}}}$. However, the absolute maximums of C_n^2 (Fig. 7d) and $Z_{i_{NP0_{sup}}}$ (indicated in Fig. 7a) correspond to an inversion around 2500 m, identified by a strong potential temperature gradient. This actually corresponds to a cloud base (see the black dots in Fig. 6) which is decoupled from the CBL. Value $Z_{i_{NP0_{std}}}$ is thus inappropriate here. There is no marked local maximum of C_n^2 at the height of Z_i estimated from the in situ radiosonde, but σ_w

(Fig. 7e) and ε (Fig. 7f) profiles have a well-marked local minimum, forming a marked local maximum on NP3.

This example illustrates the benefit of taking σ_w into account via NPx with $x > 0$ in the attribution of Z_i. It also shows the advantage of the various Z_i estimates to identify different interfaces in the case of complex vertical structure. Of course, the large complexity of this case and the weak CBL encountered in some phases of the day due to clouds and precipitation make this issue still difficult to deal with.

4.3 Clear sky with multiple layering during LIAISE

The use of the LIAISE dataset (Boone et al., 2021) allows us to test the CALOTRITON algorithm with the same UHF RWP at a different location and in different meteorological conditions. During the LIAISE campaign, the LAERO UHF RWP was deployed from June 2021 to October 2021 in the semi-arid region of Lleida, Spain, at a distance of about 15 km from large areas of irrigated crops. Figure 8 illustrates the complexity that can be observed in clear-sky conditions
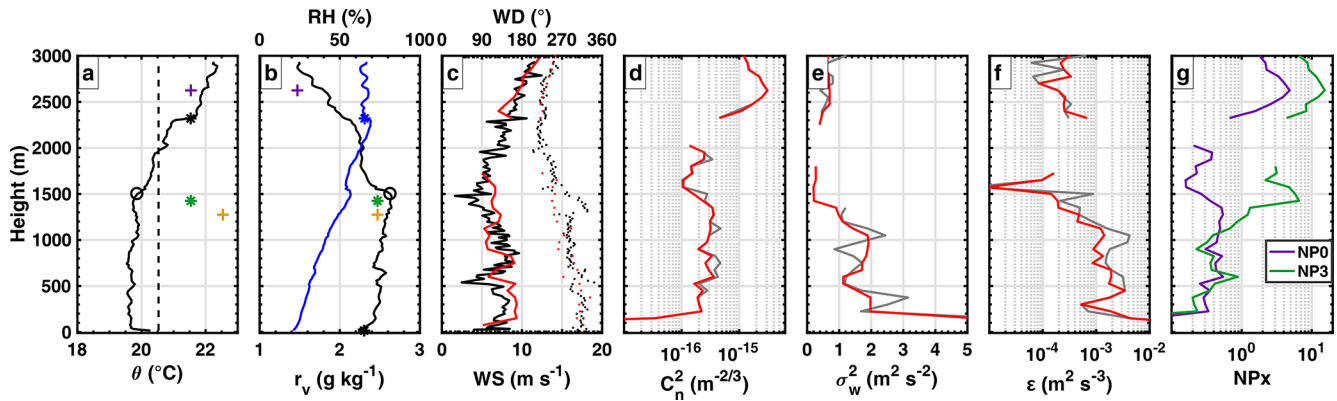
Figure 7. Same as Fig. 5 for 15 March 2018 at 14:15 UTC.

in this region and tests the capability of CALOTRITON for CBL with multilayer conditions. The analyses of this rich dataset have only recently started, but the study by Jimenez et al. (2023) already testifies to this complexity.

Early in the morning, an elevated local (actually absolute) maximum of C_n^2 is present between 2 and 3 km. This corresponds to a high inversion, potentially coming from a residual transported layer (shown later). An algorithm purely based on maximum C_n^2 would start the day with this erroneous Z_i estimate. In CALOTRITON, the process of finding the first estimate of the day at the first possible gate enables us to avoid this situation. Most of the various Z_i estimates agree until 09:30 UTC. Between 10:00 and 13:00 UTC, $Z_{i_{NP3_{sub}}}$ indicates the potential presence of a TIBL located below 1000 m, whilst at 11:00 UTC $Z_{i_{NP0_{std}}}$ is at the level of $Z_{i_{NP3_{sub}}}$ at about 600 m. Firstly, note that the maximum C_n^2 discussed previously is still present at 11:00 UTC in Fig. 8a and corresponds to a large moisture and temperature inversion. It is not thin but associated with a large change in the water vapour mixing ratio.

Figure 9 shows measurements from a radiosonde taken at this time.

In the first 1500 m, we notice the presence of two superimposed layers with constant potential temperatures and mixing ratio (Fig. 9a and b) separated by a thermal inversion at 600 m. Strictly speaking, according to the definition of the thermodynamic approach, Z_i should be located at the top of the first layer, since the surface over-adiabaticity (28 °C) theoretically does not allow a parcel of air to cross the inversion at 600 m (29 °C above). By a scalar concentration approach, Z_i could also be attributed to 600 m where a discontinuity in the mixing ratio is indeed observed. The latter is, however, not considered to be very strong, and the fact that a constant (but slightly different) mixing ratio is observed above and up to 1300 m indicates mixing within this upper layer. An earlier sounding at 10:00 UTC (not shown here) reveals that the CBL was well mixed up to 1200 m a.g.l. on this day over this dry site. What is seen at 11:00 UTC in Fig. 9a and b is an in-

trusion of a nearby boundary layer likely advected into the region from the north-east, that is from the irrigated site, which has much thinner CBL. The cooler and moister air observed over the dry site in Fig. 8b up to 600 m is consistent with air coming from the irrigated area. In this case, that is over Els Plans, some turbulence structures may be able to overcome the 600 m high inversion and some others may not. We indeed find high turbulence values ($\varepsilon > 5 \times 10^{-4}$ m^2 s^{-3}) up to 600 m. This turbulence contributes to the mixing of both layers and eroding the inversion. This is observed later in the soundings (not shown). Comparing the 11:00 UTC radiosonde profile with the UHF RWP estimates, $Z_{i_{NP3_{std}}}$ defines Z_i at 1300 m with the presence of a TIBL inside, whose top would be located at 600 m and detected by $Z_{i_{NP3_{sub}}}$ and $Z_{i_{NP0_{std}}}$.

In Fig. 8b–c, shortly after 13:00 UTC we notice a sudden increase in turbulence up to about 2000 m a.g.l. This may be due to another boundary layer advection as the wind direction (not shown) suddenly changes from ~ 200 to $\sim 90°$ between ~ 1000 and ~ 2000 m. A break in the temporal continuity of NP3 local maxima is then observed, and the imposed growth limit does not allow us to follow this sudden evolution. The use of Z_{i_ε} (1875 m at 13:15 UTC) allows for the attributions of $Z_{i_{NP3_{std}}}$ and $Z_{i_{NP0_{std}}}$ to follow this rapid change from 975 m at 13:10 UTC to 1800 m at 13:20 UTC. From 14:00 UTC onwards, a low-level marine breeze (< 500 m) can be seen in Fig. 8a and b. This marine air is called "La Marinada" in this region (Jimenez et al., 2023) and is typical of the area. It is an entrance of marine air coming from the Mediterranean Sea, which is usually favoured by a continental heat low over northern Spain. Between 15:00 and 16:00 UTC, differences between $Z_{i_{NP3_{std}}}$ and $Z_{i_{NP0_{std}}}$ are observed, showing the high complexity of the atmosphere. After 16:00 UTC, all the attributions are made at 225 m on the first UHF RWP gate.

Figure 10 shows the data from a radiosonde launched at 18:00 UTC on the same day, where it can be seen that $Z_{i_{NP3_{std}}}$ and $Z_{i_{NP0_{std}}}$ are well established at the height of the maxi-
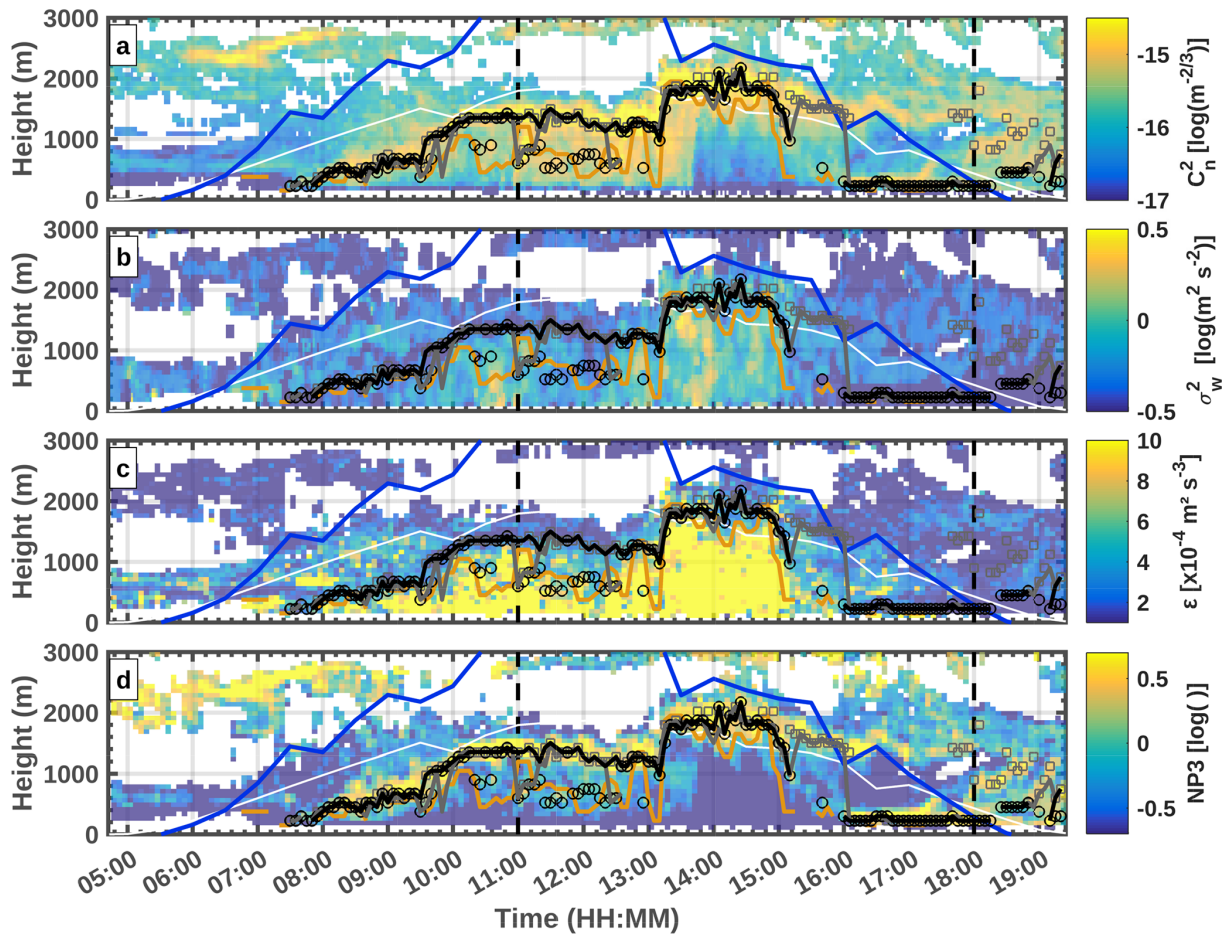
Figure 8. LAERO UHF RWP observations for 27 July 2021 at Els Plans (Spain) during the LIAISE campaign with the same description as Fig. 4.
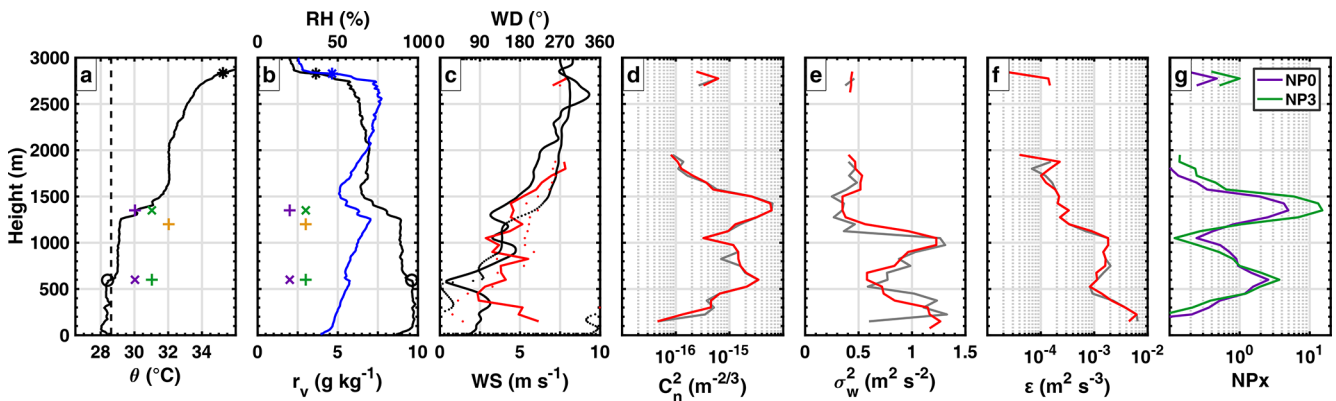
Figure 9. Same as Fig. 5 but with profiles measured by radiosounding and LAERO UHF RWP at Els Plans (Spain) during the LIAISE campaign on 27 July 2021 at 11:00 UTC.

mum potential temperature and mixing ratio gradient. The observed breeze has therefore set up a new convective boundary layer.

At 19:00 UTC, the radiosonde data (not shown) indicate that Z_i decreases below the first reliable RWP gate;

CALOTRITON attributions are then erroneously overestimated by about 500 m a.g.l.

This example has shown a highly complex situation, which can occur even in clear-sky conditions. It exemplifies the complexity of automatically assigning Z_i with radiosonde

data or remote sensing when several boundary layers interact and lead to multilayering in the lower troposphere. It also illustrates how the different CALOTRITON attributions can help to identify CBL top, TIBL top, and the advection of internal boundary layers. The flag defined in Sect. 3.3.3 helps to identify the days when this kind of complex layering of the low troposphere may occur.

5 Validation of CALOTRITON with in situ measurements

The previous sections have shown that $Z_{i_{\mathrm{NP3_{std}}}}$ gives the best estimates of Z_i. To validate this estimate, all CALOTRITON attributions were compared to the numerous radiosonde data made during the LIAISE and BLLAST field experiments near two UHF RWPs (Table 1). During BLLAST, the LAERO UHF RWP was at P2OA-CRA, and the CNRM UHF RWP was about 5 km to the south. RPAS (Reuder et al., 2016) profiles were made near the two sites, and radiosounding balloons were launched from both sites (Lothon et al., 2014; Legain et al., 2013), a few tens of metres from the RWPs. During LIAISE, the LAERO UHF RWP was installed on a dry area (Els Plans) and the CNRM UHF RWP was installed on an irrigated area (La Cendrosa) (see Sect. 4.3) about 15 km away (Boone et al., 2021). Radiosoundings were launched from the two sites as well, near the RWPs (also a few tens of metres away). A total of about 500 profiles are available for the evaluation of the CALOTRITON estimates. Median filters are applied over the vertical to the in situ data to match a vertical resolution of 10 m. Those numerous in situ profiles give the opportunity to evaluate and validate CALOTRITON and also give some insight into the results from automatic estimates from thermodynamic profiles.

In Fig. 11a–b, we compare $Z_{i_{\mathrm{NP3_{std}}}}$ with automatic in situ estimates based respectively on the parcel method (one of the most frequently used methods) and on the water vapour mixing ratio gradient method (as an example of the gradient method).

In the parcel method, a small amount $\delta\theta$ is added to the surface potential temperature (θ_s), and $Z_{i_{\mathrm{parcel}}}$ is defined as the height where $\theta = \theta_s + \delta\theta$ above the surface (Seibert et al., 2000). Here we set $\delta\theta$ to 0.25 °C (Fig. 5a). A great disparity in points is observed, which is mainly explained by a poor estimation of $Z_{i_{\mathrm{parcel}}}$ in non-textbook cases. They are indeed either overestimated (example in Fig. 7a) or underestimated by the potential presence of TIBL (example in Fig. 9a). Value $\delta\theta$ may not always be appropriate, according to the actual super-adiabatism close to surface. In addition, a large number of small Z_i estimates by the parcel method (< 200 m) can be observed due to the observation of a positive potential temperature gradient in the very first metres of the profiles. Hennemuth and Lammert (2006) attribute this to evening transitions, but it may actually happen at any time (see Fig. 9a),

for example, by the establishment of local breezes or other types of advection. It can also occur when the surface layer is not clear (showing fluctuations over the vertical) during the start and at the spot of the sounding. The parcel method may or may not be fair in those cases. The in situ radiosounding or RPAS profile are very local and instantaneous. Note that using the bulk Richardson method rather than the parcel method did not significantly change the result of this comparison (not shown). The bulk Richardson Z_i estimates were actually slightly less relevant than the parcel method estimates with more frequent overestimation of Z_i due to the attribution of Z_i on upper inversions.

The in situ-based gradient methods assign Z_i at the height of the strongest gradient of potential temperature, water vapour mixing ratio, or relative humidity below 3000 m. Figure 11b shows the comparison between $Z_{i_{\mathrm{NP3_{std}}}}$ and the water vapour mixing ratio gradient estimates. There is a large majority of cases where attributions based on the water vapour mixing ratio gradient method ($Z_{i_{r_v\,\mathrm{gradient}}}$) are largely above $Z_{i_{\mathrm{NP3_{std}}}}$. They mostly correspond to attributions to residual layers or upper inversion, as described by Hennemuth and Lammert (2006) and as seen in the previous examples (Figs. 7 and 9). Furthermore, a significant number of attributions by gradient methods are very low and correspond not only to the stable surface layer (around morning or evening transitions), but also to the fact that one can observe large fluctuations in the surface layer as seen in Fig. 7b. Similar results are found when considering the potential temperature or the relative humidity for the gradient method (not shown).

Figure 11a–b show that it remains difficult to qualify CALOTRITON estimates with the automatically determined estimates from in situ parcel or gradient methods. For this reason, a subjective method of assigning Z_i from in situ thermodynamical profiles is helpful. We attempt to keep this method as objective as possible by assigning Z_i at the height where we observe the first notable discontinuity in the mixing ratio profile associated with discontinuity in the potential temperature profile. The approach is similar to searching for the top of a conserved scalar tracer, and it should also correspond to the height where the entrainment zone starts (see Fig. 1d). Figure 11c shows the comparison of this subjective Z_i with CALOTRITON estimates based on NP3$_{\mathrm{std}}$. We obtain a much better agreement between the attributions with a higher regression coefficient ($R^2 = 0.57$), but some points still deviate from the trend, and this may be due to subjective misinterpretation as we have seen in the presence of TIBL, for example, or due to the failure of CALOTRITON estimates.

In order to disregard errors in the in situ estimates, we finally restrict the comparison of $Z_{i_{\mathrm{NP3_{std}}}}$ with in situ estimates to the cases where the standard deviation within the estimates from the various in situ methods is lower than 100 m. This way, we ensure consistency between those methods; that is, we keep the more "simple" or "textbook" situations. We also ensure objectivity. Figure 11d shows an excellent comparison
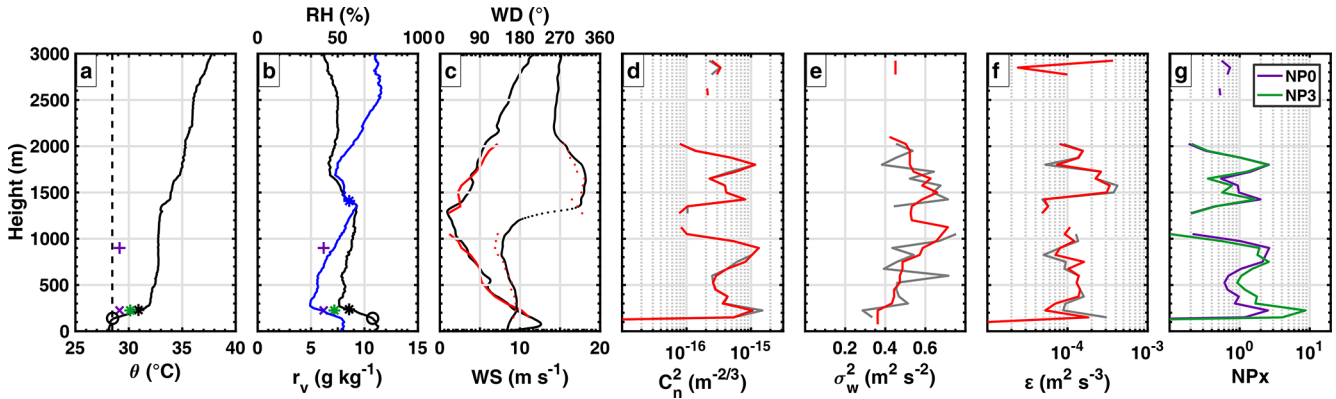
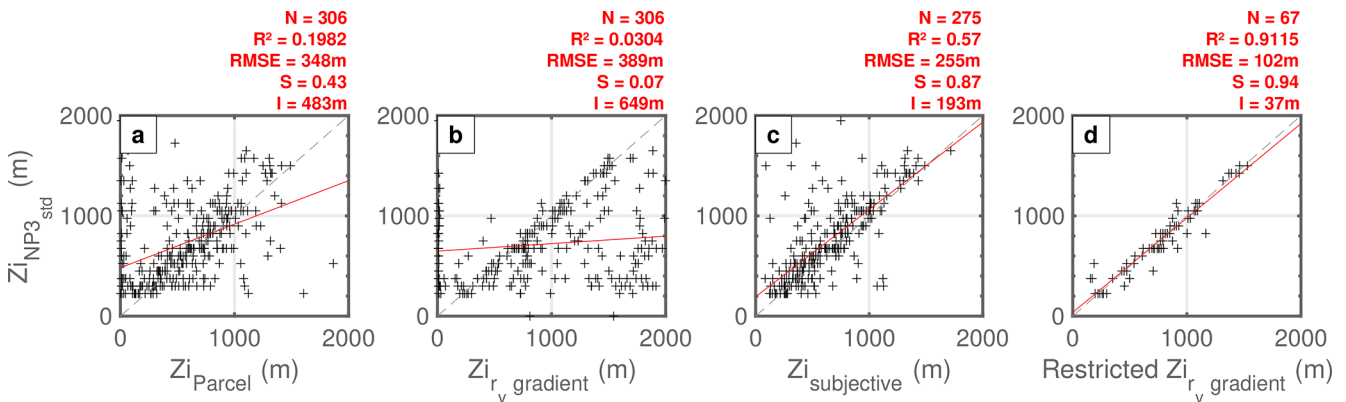**Figure 10.** Same as Fig. 9 but at 18:00 UTC.

Figure 11. Comparison between $Z_{i_{\mathrm{NP3_{std}}}}$ and **(a)** Z_i from the in situ parcel method, **(b)** Z_i from the in situ water vapour mixing ratio gradient method, **(c)** subjective Z_i estimates, and **(d)** restricted Z_i from the convergence of all the in situ-based estimates. In all panels, the dashed grey line represents the 1 : 1 slope, and the red line is the linear regression. The characteristics of the regression are indicated in red: the number of data points (N), the regression coefficient (R^2), the root-mean-square error (RMSE), the regression slope (S), and the intercept (I).

between $Z_{i_{\mathrm{NP3_{std}}}}$ and Z_i from the in situ mixing ratio gradient method in those conditions, with $R^2 = 0.91$ and a root-mean-square error (RMSE) of 102 m. However, there are still a few points that deviate, which is mainly due to

– late afternoon conditions, when the atmosphere starts to stabilize in the surface layer (In these cases, we are actually at the limit of the CBL definition);

– attributions below the UHF RWP vertical detection limitation.

If we ignore in situ attributions below 225 m and at times later than 16:00 UTC, we obtain $R^2 = 0.93$ and RMSE = 84 m (which is close to the 75 m UHF RWP vertical resolution), which confirms the consistency of CALOTRITON estimates in those conditions.

Table 5 summarizes all the comparisons made between the UHF RWP CALOTRITON estimates (based on various orders of NPx in standard configuration as described in Table 4) and in situ estimates (based on the different methods).

$Z_{i_{\mathrm{NP4_{std}}}}$ has slightly larger R^2 and a lower RMSE when compared with the subjective in situ Z_i estimates. However, generally, NP3$_{\mathrm{std}}$-based attributions are very similar to NP4$_{\mathrm{std}}$-based attributions and, moreover, lead to 4 % more attributions when compared to the subjective-method in situ estimates. This further supports the optimum choice of using $Z_{i_{\mathrm{NP3_{std}}}}$ to estimate Z_i with CALOTRITON and the validity of those estimates. Finally, when we compare the attributions of NP3$_{\mathrm{std}}$ with QF = 1 with those of restricted $Z_{i_{\mathrm{rv\,gradient}}}$, which both reflect a simple textbook case, the results are excellent with an R^2 of more than 0.96 and an RMSE = 71 m, which is lower than the RWP vertical resolution (75 m).

In conclusion, we also show that CALOTRITON is not specific to one UHF RWP and one observational site.

6 Summary and discussion

With this new algorithm, the main objective of obtaining reliable estimates of Z_i with a UHF RWP for the analysis of

Table 5. Summary of linear regression characteristics between Z_i from CALOTRITON with NPx ($x = 0$ to $x = 5$) in standard configuration as described in Table 4 and Z_i from the in situ subjective method; restricted Z_i estimates based on the in situ mixing ratio gradient method, agreeing with other in situ-based estimates as described in the text; and the same Z_i with further restrictions (no attributions below 225 m or after 16:00 UTC).

Compared $Z_{i_{NPx_{config}}}$	$Z_{i_{NP0_{std}}}$	$Z_{i_{NP1_{std}}}$	$Z_{i_{NP2_{std}}}$	$Z_{i_{NP3_{std}}}$	$Z_{i_{NP4_{std}}}$	$Z_{i_{NP5_{std}}}$	$Z_{i_{NP3_{std}}}$ (QF = 1)
With $Z_{i_{subjective}}$							
Number of data points	288	284	286	275	264	254	142
R^2	0.43	0.56	0.47	0.57	0.59	0.56	0.62
RMSE	285 m	246 m	309 m	255 m	253 m	270 m	255 m
Slope	0.74	0.85	0.86	0.87	0.89	0.89	0.9
Intercept	219 m	162 m	204 m	193 m	193 m	200 m	150 m
With restricted $Z_{i_{r_v gradient}}$							
Number of data points	70	70	69	67	66	62	39
R^2	0.72	0.80	0.70	0.91	0.88	0.87	0.94
RMSE	181 m	149 m	182 m	102 m	117 m	126 m	90 m
Slope	0.84	0.87	0.81	0.94	0.90	0.94	0.96
Intercept	65 m	68 m	69 m	37 m	76 m	47 m	5 m
With restricted $Z_{i_{r_v gradient}}$ and without $Z_i < 225$ m and only before 16:00 UTC							
Number of data points	56	56	55	52	52	49	29
R^2	0.70	0.80	0.81	0.93	0.93	0.92	0.96
RMSE	179 m	138 m	135 m	84 m	79 m	95 m	71 m
Slope	0.97	0.99	0.99	1.03	1.02	1.07	1.03
Intercept	−55 m	−38 m	−34 m	−42 m	−33 m	−68 m	−43 m

Table 6. Summary of the instruments and datasets used.

Instrument	Context	Location	Period	DOI reference
LAERO UHF RWP	P2OA	Campistrous, France	2015–2022	Lothon (2023a)
LAERO UHF RWP	BLLAST	Campistrous, France	June–July 2011	Saïd (2012)
LAERO UHF RWP	LIAISE	Els Plans, Spain	July 2021	Lothon and Vial (2022)
CNRM UHF RWP	BLLAST	Capvern, France	June–July 2011	Garrouste (2011)
CNRM UHF RWP	LIAISE	La Cendrosa, Spain	July 2021	Lothon (2023b)
CT25k ceilometer	P2OA	Campistrous, France	2016–2019	Contact author
Sonic anemometer	P2OA	Campistrous, France	2015–2022	Lohou et al. (2023a, b)
Sonic anemometer	BLLAST	Campistrous, France	June–July 2011	Lohou (2017)
Sonic anemometer	LIAISE	Els Plans, Spain	July 2021	Price (2023a)
Sonic anemometer	LIAISE	La Cendrosa, Spain	July 2021	Canut et al. (2022)
Radiosoundings	BLLAST	Campistrous, France	June–July 2011	Lothon (2018)
Radiosoundings	BLLAST	Capvern, France	June–July 2011	Legain (2011)
Radiosoundings	LIAISE	Els Plans, Spain	July 2021	Price (2023b)
Radiosoundings	LIAISE	La Cendrosa, Spain	July 2021	Garrouste et al. (2022)
RPAS	BLLAST	Campistrous, France	June–July 2011	Reuder and Jonassen (2017)

long-term series is met here, except for CBL thinner than 225 m.

CALOTRITON uses two surface sensors in addition to the RWP: a humidity sensor at 2 m and a sonic anemometer for the evaluation of the sensible heat flux. We have seen that CALOTRITON can give satisfying results without the sensible heat flux input. The use of the humidity sensor allows for strong restriction of the attributions, especially in the presence of low stratus and fog. It thus remains useful and a low-cost and easy-to-use input. If this sensor is missing, CALOTRITON will likely attribute inaccurate Z_i estimates on the top of the fog when it occurs. Using the sensible heat flux to restrict the estimations to days with significant fluxes (for example larger than $50\,\mathrm{W\,m^{-2}}$) can help to avoid the difficult CBL detection in winter (with very shallow or nonexistent CBL) or in certain strong foehn or heat wave cases (when the sensible heat fluxes may be low or even negative).

Relatively to the simpler, previously used algorithms for this profiler and to standard methods, CALOTRITON manages to deal with quite complex cases. Those "standard methods" are mainly based on catching the appropriate local maximum of C_n^2 with the help of temporal continuity. In CALOTRITON, the search for the first attribution of Z_i at the first reliable UHF RWP gate is a significant progress consistent with the approach of Molod et al. (2015). Furthermore, taking into account both the higher reflectivity at inversions and the amount of turbulence within the CBL by use of the new key variable NPx allows for improvement in the attributions, in particular in the presence of clouds (the value of x being 3 or 4 seems the most appropriate). This was also found by Bianco and Wilczak (2002) with a different innovative fuzzy logic approach.

The criterion of temporal continuity, which appears as a real need, sometimes induces errors. Indeed, the associated jump threshold that is tolerated for CBL growth is somehow arbitrary and prevents the potential abrupt growth in certain conditions. Using Z_{i_ε} to allow for a higher growth limit in those specific conditions helps to better manage complex cases. This is another improvement introduced by CALOTRITON. However, this one can also induce errors, in particular in the morning, by attributing Z_i at the height of residual layers. Using an additional median filter on Z_{i_ε} could allow us to limit these errors by better considering a certain temporal continuity of Z_{i_ε}. The definition of Z_{i_ε} could itself be improved. It is by itself an interesting useful variable.

The comparison of CALOTRITON Z_i estimates with in situ thermodynamic profiles has shown that there is no automatic method based on in situ thermodynamic profiles which can deal with the complexity of the atmospheric structure and that the subjective method remains the best one. Such a subjective approach was actually also considered to be a reference in Bianco et al. (2008) but applied to the RWP variables.

CALOTRITON is definitely not a simple algorithm, but this actually reveals the need to adapt to the high complexity of the lower-atmosphere vertical structure. Bianco et al. (2008) proposed an improved algorithm relative to Bianco and Wilczak (2002) with more complexity added, which demonstrates this need for complexity and adjustments to optimize the understanding and detection of the appropriate interface. The flag system and various types of Z_i estimates proposed in CALOTRITON allow us to express and document this vertical structure complexity while giving information on the quality and difficulty of the Z_i estimations. In complex cases, characterizing the convective boundary layer by a single height may actually not be appropriate, in particular in the presence of TIBL, where it is difficult to determine (and even define) Z_i even based on in situ thermodynamical data. It becomes very difficult to statistically qualify CALOTRITON attributions in such cases. Over the 8-year time series of the UHF RWP at P2OA, we find that 17 % of the days have more than 75 % of their Z_i estimates with QF = 1. This means that about 17 % of the days are quite close to textbook cases, with high confidence in CALOTRITON Z_i estimates. In contrast, at Els Plans during the LIAISE campaign none of the days present QF = 1 for more than 75 % of the time of day. That is why there is no simple textbook case in this area during the LIAISE summer campaign.

The use of the different Z_i estimates by CALOTRITON is also of large interest for documenting the complex structure of the CBL, like the one found both in P2OA (at the foothills of the Pyrenees ridge) and at LIAISE (with the influence of the sea and the mountain at mesoscale). Moreover, it should only be used for statistical purposes with caution. One can, for example, estimate the occurrence of significant differences between $Z_{i_{\mathrm{NP3_{std}}}}$ and $Z_{i_{\mathrm{NP3_{sub}}}}$. At P2OA during the 8-year time series we find that only 3 % of the days show a significant difference between both estimates for more than 25 % of the time. This would mean that TIBLs are not very frequent at P2OA. In contrast, at Els Plan during LIAISE we find that 26 % of the days to be this way, which likely means that TIBLs occurred very frequently during the LIAISE campaign. One can also estimate the occurrence of differences between $Z_{i_{\mathrm{NP3_{std}}}}$ and $Z_{i_{\mathrm{NP0_{sup}}}}$; at P2OA, over the 8-year time series, 72 % of the days show a significant difference between both variables for more than 25 % of each day. Those days can be related to the high occurrence of cloud layers above the CBL top, which generate inversions. At Els Plans during LIAISE this number reaches 92 %, which likely means that there are established upper inversions in the LIAISE area. Those preliminary statistics reveal the high complexity of the LIAISE study area and the potential of the CALOTRITON various estimates and flags. However, case-by-case studies and further analyses are needed to help us with qualifying this potential.

Author contributions. AP is the main author of the CALOTRITON algorithm, tackling conception, coding, tests, evaluation, and data analysis. He is also the main writer of the article. ML supervised the work and analysis and helped with the writing. She is the principal investigator of the Laboratoire d'Aérologie's ultra-high-frequency radar wind profiler (LAERO UHF RWP). JA and PYM are the co-ordinators of the funding contract and collaborated to do the work. BC is the author of the initial code for the UHF RWP data process and of the previous algorithm for Z_i estimates. He helped with the algorithm conception. SD is responsible for the P2OA-CRA instrumentation and data. She and AV helped with the instrumentation maintenance, data process, and data availability. YB operated the LAERO UHF RWP at P2OA and during field experiments and helped with the operation of the CNRM UHF RWP during LIAISE. FL is the principal investigator of the 60 m tower and contributed to the writing. GC was the lead of the instrumental deployment during LIAISE and especially of the CNRM instruments installed at La Cendrosa. JB was responsible for the deployment of radiosoundings at Els Plans during LIAISE and contributed to the writing. JR was the PI of SUMO RPAS during BLLAST and contributed to the writing.

References

Angevine, W. M.: Atmospheric boundary layer height measurements with wind profilers: Successes and cautions, International Geoscience and Remote Sensing Symposium (IGARSS), 1, 197–198, https://doi.org/10.1109/igarss.2000.860466, 2000.

Angevine, W. M., White, A. B., and Avery, S. K.: Boundary-layer depth and entrainment zone characterization with a boundary-layer profiler, Bound.-Lay. Meteorol., 68, 375–385, https://doi.org/10.1007/BF00706797, 1994.

Bianco, L. and Wilczak, J. M.: Convective boundary layer depth: Improved measurement by Doppler radar wind profiler using fuzzy logic methods, J. Atmos. Ocean. Technol., 19, 1745–1758, https://doi.org/10.1175/1520-0426(2002)019<1745:CBLDIM>2.0.CO;2, 2002.

Bianco, L., Wilczak, J. M., and White, A. B.: Convective boundary layer depth estimation from wind profilers: Statistical comparison between an automated algorithm and expert estimations, J. Atmos. Ocean. Technol., 25, 1397–1413, https://doi.org/10.1175/2008JTECHA981.1, 2008.

Blay-Carreras, E., Pino, D., Vilà-Guerau de Arellano, J., van de Boer, A., De Coster, O., Darbieu, C., Hartogensis, O., Lohou, F., Lothon, M., and Pietersen, H.: Role of the residual layer and large-scale subsidence on the development and evolution of the convective boundary layer, Atmos. Chem. Phys., 14, 4515–4530, https://doi.org/10.5194/acp-14-4515-2014, 2014.

Boone, A., Bellvert, J., Best, M., Brooke, J., Canut-Rocafort, G., Cuxart, J., Hartogensis, O., Le Moigne, P., Miró, J. R., Polcher, J., Price, J., Quintana Seguí, P., and Wooster, M.: Updates on the international Land Surface Interactions with the Atmosphere

over the Iberian Semi-Arid Environment (LIAISE) Field Campaign, Gewex News, 31, 17–21, 2021.

Caicedo, V., Rappenglück, B., Lefer, B., Morris, G., Toledo, D., and Delgado, R.: Comparison of aerosol lidar retrieval methods for boundary layer height detection using ceilometer aerosol backscatter data, Atmos. Meas. Tech., 10, 1609–1622, https://doi.org/10.5194/amt-10-1609-2017, 2017.

Canut, G., Garrouste, O., and Etienne, J.-C.: LIAISE LA-CENDROSA CNRM MTO-1MIN L2, AERIS [data set], https://doi.org/10.25326/33, 2022.

Cohn, S. A. and Angevine, W. M.: Boundary Layer Height and Entrainment Zone Thickness Measured by Lidars and Wind-Profiling Radars, J. Appl. Meteorol., 39, 1233–1247, https://doi.org/10.1175/1520-0450(2000)039<1233:BLHAEZ>2.0.CO;2, 2000.

Collaud Coen, M., Praz, C., Haefele, A., Ruffieux, D., Kaufmann, P., and Calpini, B.: Determination and climatology of the planetary boundary layer height above the Swiss plateau by in situ and remote sensing measurements as well as by the COSMO-2 model, Atmos. Chem. Phys., 14, 13205–13221, https://doi.org/10.5194/acp-14-13205-2014, 2014.

Compton, J. C., Delgado, R., Berkoff, T. A., and Hoff, R. M.: Determination of planetary boundary layer height on short spatial and temporal scales: A demonstration of the covariance wavelet transform in ground-based wind profiler and lidar measurements, J. Atmos. Ocean. Technol., 30, 1566–1575, https://doi.org/10.1175/JTECH-D-12-00116.1, 2013.

Couvreux, F., Bazile, E., Canut, G., Seity, Y., Lothon, M., Lohou, F., Guichard, F., and Nilsson, E.: Boundary-layer turbulent processes and mesoscale variability represented by numerical weather prediction models during the BLLAST campaign, Atmos. Chem. Phys., 16, 8983–9002, https://doi.org/10.5194/acp-16-8983-2016, 2016.

Davis, K. J., Gamage, N., Hagelberg, C., Kiemle, C., Lenschow, D., and Sullivan, P.: An objective method for deriving atmospheric structure from airborne lidar observations, J. Atmos. Ocean. Technol., 17, 1455–1468, https://doi.org/10.1175/1520-0426(2000)017<1455:AOMFDA>2.0.CO;2, 2000.

Deardorff, J. W.: Theoretical expression for the countergradient vertical heat flux, J. Geophys. Res., 77, 5900–5904, https://doi.org/10.1029/jc077i030p05900, 1972.

Doviak, R. and Zrnic, D.: Doppler Radar and Weather Observations, Elsevier, ISBN 9780122214226, https://doi.org/10.1016/C2009-0-22358-0, 1993.

Duncan Jr., J. B., Bianco, L., Adler, B., Bell, T., Djalalova, I. V., Riihimaki, L., Sedlar, J., Smith, E. N., Turner, D. D., Wagner, T. J., and Wilczak, J. M.: Evaluating convective planetary boundary layer height estimations resolved by both active and passive remote sensing instruments during the CHEESEHEAD19 field campaign, Atmos. Meas. Tech., 15, 2479–2502, https://doi.org/10.5194/amt-15-2479-2022, 2022.

Durand, P., Druilhet, A., and Briere, S.: A Sea-Land Transition Observed during the COAST Experiment, J. Atmos. Sci., 46, 96–116, https://doi.org/10.1175/1520-0469(1989)046<0096:ASLTOD>2.0.CO;2, 1989.

Frehlich, R., Meillier, Y., Jensen, M. L., Balsley, B., and Sharman, R.: Measurements of Boundary Layer Profiles in an Urban Environment, J. Appl. Meteorol. Climatol., 45, 821–837, https://doi.org/10.1175/JAM2368.1, 2006.

Garrouste, O.: UHF CNRM Site 2, AERIS [data set], https://doi.org/10.6096/bllast.uhf.site2, 2011.

Garrouste, O., Canut, G., and Roy, A.: LIAISE LA-CENDROSA CNRM RS L2, AERIS [data set], https://doi.org/10.25326/322, 2022.

Grimsdell, A. W. and Angevine, W. M.: Convective boundary layer height measurement with wind profilers and comparison to cloud base, J. Atmos. Ocean. Technol., 15, 1331–1338, https://doi.org/10.1175/1520-0426(1998)015<1331:CBLHMW>2.0.CO;2. , 1998.

Grimsdell, A. W. and Angevine, W. M.: Observations of the Afternoon Transition of the Convective Boundary Layer, J. Appl. Meteorol., 41, 3–11, https://doi.org/10.1175/1520-0450(2002)041<0003:OOTATO>2.0.CO;2, 2002.

Haeffelin, M., Angelini, F., Morille, Y., Martucci, G., Frey, S., Gobbi, G. P., Lolli, S., O'Dowd, C. D., Sauvage, L., Xueref-Rémy, I., Wastine, B., and Feist, D. G.: Evaluation of Mixing-Height Retrievals from Automatic Profiling Lidars and Ceilometers in View of Future Integrated Networks in Europe, Bound.-Lay. Meteorol., 143, 49–75, https://doi.org/10.1007/s10546-011-9643-z, 2012.

Hanna, S. R.: The thickness of the planetary boundary layer, Atmos. Environ., 3, 519–536, https://doi.org/10.1016/0004-6981(69)90042-0, 1969.

Hennemuth, B. and Lammert, A.: Determination of the atmospheric boundary layer height from radiosonde and lidar backscatter, Bound.-Lay. Meteorol., 120, 181–200, https://doi.org/10.1007/s10546-005-9035-3, 2006.

Heo, B. H., Jacoby-Koaly, S., Kim, K. E., Campistron, B., Benech, B., and Jung, E. S.: Use of the Doppler spectral width to improve the estimation of the convective boundary layer height from UHF wind profiler observations, J. Atmos. Ocean. Technol., 20, 408–424, https://doi.org/10.1175/1520-0426(2003)020<0408:UOTDSW>2.0.CO;2, 2003.

Holzworth, G. C.: Estimates of mean maximum mixing depths in the contiguous united states, Mon. Weather Rev., 92, 235–242, https://doi.org/10.1175/1520-0493(1964)092<0235:EOMMMD>2.3.CO;2, 1964.

Jacoby-Koaly, S.: Application d'un radar profileur de vent UHF à l'étude de la couche limite atmosphérique, Ph.D. thesis, thèse de doctorat dirigée par Campistron, Bernard Physique de l'atmosphère Toulouse 3 2000, http://www.theses.fr/2000TOU30144 (last access: 22 March 2024), 2000.

Jacoby-Koaly, S., Campistron, B., Bernard, S., Bénech, B., Ardhuin-Girard, F., Dessens, J., Dupont, E., and Carissimo, B.: Turbulent Dissipation Rate In The Boundary Layer Via UHF Wind Profiler Doppler Spectral Width Measurements, Bound.-Lay. Meteorol., 103, 361–389, https://doi.org/10.1023/A:1014985111855, 2002.

Jiménez, M. A., Grau, A., Martínez-Villagrasa, D., and Cuxart, J.: Characterization of the marine-air intrusion Marinada in the eastern Ebro sub-basin, Int. J. Climatol., 43, 7682–7699. https://doi.org/10.1002/joc.8287, 2023.

Kossmann, M., Gtlin, R. V., Corsmeier, U., Vogel, B., Fiedler, F., Binder, H.-J., Kalthoff, N., and Beyrich, F.: Aspects of the convective boundary layer structure over complex terrain, Atmos. Environ., 32, 1323–1348, https://doi.org/10.1016/S1352-2310(97)00271-9, 1998.

Kotthaus, S., Bravo-Aranda, J. A., Collaud Coen, M., Guerrero-Rascado, J. L., Costa, M. J., Cimini, D., O'Connor, E. J., Hervo, M., Alados-Arboledas, L., Jiménez-Portaz, M., Mona, L., Ruffieux, D., Illingworth, A., and Haeffelin, M.: Atmospheric boundary layer height from ground-based remote sensing: a review of capabilities and limitations, Atmos. Meas. Tech., 16, 433–479, https://doi.org/10.5194/amt-16-433-2023, 2023.

Legain, D.: Frequent radiosoundings Site 2, AERIS [data set], https://doi.org/10.6096/bllast.frequentsoundingssite2, 2011.

Legain, D., Bousquet, O., Douffet, T., Tzanos, D., Moulin, E., Barrie, J., and Renard, J.-B.: High-frequency boundary layer profiling with reusable radiosondes, Atmos. Meas. Tech., 6, 2195–2205, https://doi.org/10.5194/amt-6-2195-2013, 2013.

Liu, Z., Barlow, J. F., Chan, P.-W., Fung, J., Li, Y., Ren, C., Mak, H., and Ng, E.: A Review of Progress and Applications of Pulsed Doppler Wind LiDARs, Remote Sens., 11, 2522, https://doi.org/10.3390/rs11212522, 2019.

Lohou, F.: Meteorological parameters and flux, AERIS [data set], https://doi.org/10.6096/bllast.60mtower.meteo, 2017.

Lohou, F., Derrien, S., Vial, A., Philibert, A., Gabella, O., Said, F., Pique, E., and Meyerfeld, Y.: P2OA-CRA station – Turbulence measurements – L2A, ERIS, https://doi.org/10.25326/550, 2023a.

Lohou, F., Derrien, S., Vial, A., Philibert, A., Gabella, O., Said, F., Pique, E., and Meyerfeld, Y.: 60 m Tower – P2OA-CRA station – Meteorological variables – L2A, AERIS [data set], https://doi.org/10.25326/551, 2023b.

Lothon, M.: MODEM Radiosoundings Site 1, AERIS [data set], https://doi.org/10.6096/bllast.modem, 2018.

Lothon, M.: UHF-RADAR – P2OA-CRA station – Level 2A wind profiles – Monthly files, AERIS [data set], https://doi.org/10.25326/563, 2023a.

Lothon, M.: LIAISE LA-CENDROSA CNRM UHFWindProfiler-LowMode L2, AERIS [data set], https://doi.org/10.25326/471, 2023b.

Lothon, M. and Vial, A.: LIAISE ELS-PLANS LAERO UHFWindProfiler-LowMode L2, AERIS [data set], https://doi.org/10.25326/363, 2022.

Lothon, M., Lenschow, D. H., and Mayor, S. D.: Coherence and scale of vertical velocity in the convective boundary layer from a Doppler lidar, Bound.-Lay. Meteorol., 121, 521–536, https://doi.org/10.1007/s10546-006-9077-1, 2006.

Lothon, M., Lohou, F., Pino, D., Couvreux, F., Pardyjak, E. R., Reuder, J., Vilà-Guerau de Arellano, J., Durand, P., Hartogensis, O., Legain, D., Augustin, P., Gioli, B., Lenschow, D. H., Faloona, I., Yagüe, C., Alexander, D. C., Angevine, W. M., Bargain, E., Barrié, J., Bazile, E., Bezombes, Y., Blay-Carreras, E., van de Boer, A., Boichard, J. L., Bourdon, A., Butet, A., Campistron, B., de Coster, O., Cuxart, J., Dabas, A., Darbieu, C., Deboudt, K., Delbarre, H., Derrien, S., Flament, P., Fourmentin, M., Garai, A., Gibert, F., Graf, A., Groebner, J., Guichard, F., Jiménez, M. A., Jonassen, M., van den Kroonenberg, A., Magliulo, V., Martin, S., Martinez, D., Mastrorillo, L., Moene, A. F., Molinos, F., Moulin, E., Pietersen, H. P., Piguet, B., Pique, E., Román-Cascón, C., Rufin-Soler, C., Saïd, F., Sastre-Marugán, M., Seity, Y., Steeneveld, G. J., Toscano, P., Traullé, O., Tzanos, D., Wacker, S., Wildmann, N., and Zaldei, A.: The BLLAST field experiment: Boundary-Layer Late Afternoon and Sunset Turbulence, Atmos.

Chem. Phys., 14, 10931–10960, https://doi.org/10.5194/acp-14-10931-2014, 2014.

Lothon, M., Gheusi, F., Lohou, F., Pont, V., Derrien, S., Bezombes, Y., Leclerc, E., Vial, A., Athier, G., Jambert, C., Gardrat, E., Andriatiana, A., Meyerfeld, Y., Campistron, B., Saïd, F., Philibert, A., Stark, F., Estrampes, J.-B., Pique, E., Guesdon, F., Bret, G., Lacassagne, F., Guesdon, L., Gueffier, J., Jeroen, S., and Zaïda, G. K.: The long-term dataset of the Pyrenean Platform for Observation of the Atmosphere, Earth Syst. Sci. Data Discuss., submitted, 2024.

Min, J.-S., Park, M.-S., Chae, J.-H., and Kang, M.: Integrated System for Atmospheric Boundary Layer Height Estimation (ISABLE) using a ceilometer and microwave radiometer, Atmos. Meas. Tech., 13, 6965–6987, https://doi.org/10.5194/amt-13-6965-2020, 2020.

Molod, A., Salmun, H., and Dempsey, M.: Estimating planetary boundary layer heights from NOAA Profiler Network wind profiler data, J. Atmos. Ocean. Technol., 32, 1545–1561, https://doi.org/10.1175/JTECH-D-14-00155.1, 2015.

Nilsson, E., Lohou, F., Lothon, M., Pardyjak, E., Mahrt, L., and Darbieu, C.: Turbulence kinetic energy budget during the afternoon transition – Part 1: Observed surface TKE budget and boundary layer description for 10 intensive observation period days, Atmos. Chem. Phys., 16, 8849–8872, https://doi.org/10.5194/acp-16-8849-2016, 2016a.

Nilsson, E., Lothon, M., Lohou, F., Pardyjak, E., Hartogensis, O., and Darbieu, C.: Turbulence kinetic energy budget during the afternoon transition – Part 2: A simple TKE model, Atmos. Chem. Phys., 16, 8873–8898, https://doi.org/10.5194/acp-16-8873-2016, 2016b.

Pino, D., Jonker, H. J. J., Arellano, J. V.-G. D., and Dosio, A.: Role of Shear and the Inversion Strength During Sunset Turbulence Over Land: Characteristic Length Scales, Bound.-Lay. Meteorol., 121, 537–556, https://doi.org/10.1007/s10546-006-9080-6, 2006.

Price, J.: LIAISE ELS-PLANS UKMO MTO-30MIN L2, AERIS [data set], https://doi.org/10.25326/430, 2023a.

Price, J.: LIAISE ELS-PLANS UKMO radiosondes L1, AERIS [data set], https://doi.org/10.25326/429, 2023b.

Reuder, J. and Jonassen, M.: SUMO, AERIS [data set], https://doi.org/10.25326/469, 2017.

Reuder, J., Båserud, L., Jonassen, M. O., Kral, S. T., and Müller, M.: Exploring the potential of the RPA system SUMO for multipurpose boundary-layer missions during the BLLAST campaign, Atmos. Meas. Tech., 9, 2675–2688, https://doi.org/10.5194/amt-9-2675-2016, 2016.

Saïd, F.: LA Site 1, AERIS [data set], https://doi.org/10.6096/bllast.uhf.site1, 2012.

Seibert, P., Beyrich, F., Gryning, S.-E., Joffre, S., Rasmussen, A., and Tercier, P.: Review and intercomparison of operational methods for the determination of the mixing height, Atmos. Environ., 34, 1001–1027, https://doi.org/10.1016/S1352-2310(99)00349-0, 2000.

Stull, R. B.: An Introduction to Boundary Layer Meteorology, Springer Netherlands, ISBN 978-90-277-2769-5, https://doi.org/10.1007/978-94-009-3027-8, 1988.

Turner, D. D. and Löhnert, U.: Ground-based temperature and humidity profiling: combining active and passive

remote sensors, Atmos. Meas. Tech., 14, 3033–3048, https://doi.org/10.5194/amt-14-3033-2021, 2021.

Wadteufel, P. and Corbin, H.: On the analysis of single-Doppler data, J. App. Meteor., 18, 523–542, https://doi.org/10.1175/1520-0450(1979)018<0532:OTAOSD>2.0.CO;2, 1979.

White, A. B.: Mixing Depth Detection Using 915-MHz Radar Reflectivity Data, Proceedings of the 8th Symposium on Meteorological Observations and Instrumentation, Anaheim, CA, American Meteorological Society, 45 Beacon St., Boston, MA, 248–250, Anaheim, CA, USA, 1993., 1993.